JOURNAL OF PETROLOGY

Journal of Petrology, 2018, Vol. 59, No. 3, 387–418
doi: 10.1093/petrology/egy032
Advance Access Publication Date: 2 April 2018
Original Article

OXFORD

Trace Element Constraints on the Differentiation and Crystal Mush Solidification in the Skaergaard Intrusion, Greenland

Olivier Namur[1]* and Madeleine C. S. Humphreys[2]

[1]Department of Earth and Environmental Sciences, KU Leuven, Celestijnlaan 200E, 3001 Leuven, Belgium; [2]Department of Earth Sciences, Durham University, Science Labs, Durham DH1 3LE, UK

*Corresponding author. Telephone: 32 (0) 1 6376538. Fax: +32 16 32 29 80.
E-mail: olivier.namur@kuleuven.be

Received September 13, 2016; Accepted March 8, 2018

ABSTRACT

New major and trace element analyses of plagioclase and clinopyroxene in gabbros from the Skaergaard intrusion are used to understand the mechanisms of crystallization in the main magma body and in the crystal mush. Crystal cores show a continuous chemostratigraphic evolution in the Layered Series, with compatible elements (e.g. Cr and Ni in clinopyroxene) being progressively depleted from the bottom up, whereas incompatible elements (e.g. Sr, Ba, REE in plagioclase and clinopyroxene) become progressively enriched. We performed numerical models and showed that these trends can be explained by a simple process of fractional crystallization, except for the upper 20% of the intrusion where plagioclase and clinopyroxene trace element compositions depart from fractional crystallization trends. At this stage of magma chamber solidification, fractional crystallization becomes less efficient and is replaced by a major proportion of *in situ* equilibrium crystallization. Trace elements also show significant variations in interstitial overgrowths on plagioclase and clinopyroxene cumulus crystals. They result from crystallization of the interstitial liquid in the liquid + crystal mush. However, incompatible elements, and especially REE, show a degree of enrichment in plagioclase rims (> 20 ppm Ce) that strongly exceeds the highest concentrations observed in plagioclase cores (up to 4 ppm Ce) at the top of the Layered Series. Such a strong enrichment is difficult to reconcile with a simple process of fractional crystallization of the interstitial liquid in the crystal mush, but may be related to the development of silicate liquid immiscibility in the crystal mush or to delayed nucleation of apatite. After the crystallization of plagioclase and clinopyroxene overgrowths, diffusive re-equilibration during a period of 0·1–0·25 Myr significantly changed the original zoning profiles. Ce flux from clinopyroxene into the plagioclase lattice of adjacent crystals could also have contributed to the strong Ce enrichment observed in plagioclase rims.

Key words: plagioclase; zoning; crystal mush; immiscibility; cumulate; diffusion

INTRODUCTION

Formation of cumulate rocks in magma chambers starts by nucleation and growth of primocrysts (liquidus phases) which are then captured in a crystal mush made up of these primocrysts and interstitial liquid (e.g. McBirney & Noyes, 1979; Marsh, 2006; Humphreys, 2009; Holness *et al.*, 2013; Bédard, 2015). Primocrysts form at the interface between the crystal mush, comprised of previously formed crystals + interstitial melt, and the crystal-free main magma body. Although the thickness of crystal mushes (e.g. vertical section between fully-solidified cumulate rocks and the main magma body) in basaltic magma chambers and their timescales of solidification are debated (Holness *et al.*, 2007b, 2017a, 2017b, 2017c; McKenzie, 2011), their initial porosity is generally assumed to be high

($\phi = 0{\cdot}4$–$0{\cdot}6$; Irvine, 1980; Philpotts *et al.*, 1998; Jerram *et al.*, 2003). However, the formation of crystal overgrowths, crystallization of new interstitial phases and mobility of the interstitial melt either by compaction (Tegner *et al.*, 2009; McKenzie, 2011) or convection (Tait *et al.*, 1984; Toplis *et al.*, 2008) act to reduce the mush liquid fraction. These processes lead to a wide range of cumulate rocks from orthocumulates with >25 % of interstitial material (e.g. crystallized interstitial liquid) to adcumulates with <7 % of interstitial material (Wager *et al.*, 1960). Abundant studies based on experiments, modelling and analyses of natural samples have been performed to understand the mobility of the interstitial melt (Tait *et al.*, 1984; Morse, 1986; Jaupart & Tait, 1995; Meurer & Meurer, 2006; Tegner *et al.*, 2009; Humphreys, 2011; Namur & Charlier, 2012; Namur *et al.*, 2014), but a better comprehension of these processes is still hampered by our lack of detailed understanding of the physical properties of the melt (Toplis & Carroll, 1995; Tegner *et al.*, 2009; Thy *et al.*, 2009a), the rheology of the crystal mush (McKenzie, 1984, 2011; Tegner *et al.*, 2009; Namur & Charlier, 2012), and the crystal mush thickness (Holness *et al.*, 2007b, 2017a, 2017 b), as well as the rates of crystal accumulation (Morse, 2011) and crystal growth (Holness, 2015).

Few studies have investigated the geochemical evolution of the interstitial melt in a crystal mush during assumed progressive cooling and crystallization (Bernstein, 2006). Using major, minor and trace elements in plagioclase, amphibole and apatite from the Skaergaard intrusion, it was shown that, at least to some extent, the liquid inside the crystal mush evolves in a similar way to that of the liquid in the main magma body (Humphreys, 2009). In that case, intra-grain chemical variation should be identical to that observed in primocryst cores from the level of crystal capture to the top of the cumulate pile (UZc and equivalent subzones in the UBS and MBS). However, thermal buffering in the crystal mush (Namur *et al.*, 2014), chemical buffering by the crystallizing assemblage (Meurer & Claeson, 2002), reactive dissolution during melt migration (Meurer & Meurer, 2006; Lissenberg *et al.*, 2013; Namur *et al.*, 2013), and development of silicate liquid immiscibility (Humphreys, 2011) may produce geochemical trends significantly departing from that of the main magma body. In basaltic layered intrusions, most studies investigating the crystallization of the interstitial liquid in the crystal mush mush have focused on major and some minor (e.g. Ti, Fe) element compositional profiles in cumulus crystals (Toplis *et al.*, 2008; Humphreys, 2009, 2011; Namur *et al.*, 2014). No systematic *in situ* investigation of trace elements in the cores and rims of cumulus phases throughout the stratigraphy of a basaltic intrusion currently exists. The only available trace element datasets correspond to plagioclase and clinopyroxene core compositions in the Bushveld complex (Tanner *et al.*, 2014) and the Sept Iles intrusion (Namur *et al.*, 2011), core compositions and bulk mineral separates in the Skaergaard intrusion (Jang *et al.*, 2001; Jang & Naslund, 2001; McBirney, 2002) and a few trace element transects in clinopyroxene crystals from gabbronoritic plugs from East Greenland (Bernstein, 2006). Trace element data in cumulus minerals from other gabbroic intrusions (e.g. Tribuzio *et al.*, 1999, 2009; Hermann *et al.*, 2001) have been reported in the literature but were not used to discuss the crystallization of the interstitial liquid in a crystal mush. Trace elements are however extremely useful in constraining crystallization processes because they are characterized by different degrees of compatibility (Wood & Blundy, 1997; Aigner-Torres *et al.*, 2007), which can in turn evolve with the stable liquidus assemblage (Morse & Nolan, 1986), and by solid-state diffusion at magmatic and sub-solidus temperatures (Cherniak & Watson, 1994; Van Orman *et al.*, 2001; Cherniak, 2003; Cawthorn & Tegner, 2017). Trace elements incorporated in crystal overgrowths and interstitial phases may, therefore, be more sensitive than major and minor elements to important magmatic processes (Meurer & Claeson, 2002) such as crystallization of the mush liquid, melt migration and infiltration by primitive or evolved melt, reactive dissolution, as well as the timing of nucleation of new interstitial phases (Meurer & Meurer, 2006; Humphreys, 2009; Lissenberg *et al.*, 2013).

The Skaergaard intrusion, East Greenland, is considered as a case study for basaltic magmatism that crystallized as a closed system at shallow depths. Although its liquid line of descent is still debated (Wager & Brown, 1968; Hunter & Sparks, 1987; Toplis & Carroll, 1995; Thy *et al.*, 2009b), it is generally accepted that the cumulate rocks from the Skaergaard represent the crystallization products of liquids related by a common process of fractional crystallization (Wager & Brown, 1968; McBirney, 1996). At Skaergaard cumulate rocks formed at the floor (Layered Series), roof (Upper Border Series) and walls (Marginal Border Series) of the magma chamber. Primocryst assemblages are identical in the three series (Salmonsen & Tegner, 2013), but the proportion of crystallized interstitial material is generally lower in the Layered Series, especially after the appearance of cumulus Fe–Ti oxides (Tegner *et al.*, 2009; Namur *et al.*, 2014). Skaergaard rocks, therefore, span the full range from orthocumulates to adcumulates and offer a unique opportunity to discuss the processes of crystallization of the interstitial melt in a crystal mush. In this study, we present *in situ* major and trace element compositions of plagioclase and clinopyroxene in troctolites and gabbros from the Layered Series and Marginal Border Series. We show that the variation of trace elements in crystal cores with stratigraphy can, in general, be explained by a simple process of fractional crystallization. However, the evolution of some elements in the Upper Zone suggests that fractional crystallization becomes less effective in this part of the intrusion and is progressively replaced by equilibrium, *in situ*, crystallization. The evolution of trace elements during solidification of the liquid in the crystal mush and the composition of crystal rims that form during this

process are more complicated to understand. Based on trace element zoning patterns we suggest that fractional crystallization plays a major role, but that this process alone cannot fully explain the distribution of trace elements in mineral rims. This is especially true for light rare-earth elements (LREE) which show high concentrations compared to those predicted from fractional crystallization models. Such high concentrations may be related to the development of silicate liquid immiscibility in the crystal mush and/or to the timing of crystallization of modally minor phases such as apatite. We also suggest that the initial distribution of trace elements has been significantly affected by solid-state diffusion between plagioclase and clinopyroxene (Coogan & O'Hara, 2015) or plagioclase and melt. Our study confirms that crystal rims and grain boundaries are major reservoirs of incompatible elements in cumulate rocks (Hiraga *et al.*, 2004) and that the bulk rock distribution of trace elements is not only controlled by the crystallization of accessory phases (Meurer & Meurer, 2006), but also by the formation of zoned crystals. This is an important result that cannot be accessed from studies using bulk mineral separates (Jang *et al.*, 2001; Jang & Naslund, 2001; Cawthorn & Tegner, 2017).

THE SKAERGAARD INTRUSION

The Eocene Skaergaard intrusion of East Greenland occupies a box-shaped, fault-bounded, fossil magma chamber, approximately 8 km x 11 km x 4 km (Nielsen, 2004) at the contact between Precambrian gneisses and a thick overlying sequence of Eocene plateau lavas. It formed during the opening of the Northeast Atlantic $\sim$ 55 Myr ago (Hirschmann *et al.*, 1997).

The intrusion is divided into three main units: the Layered Series (LS) which crystallized on the floor, the Upper Border Series (UBS) which crystallized from the roof, and the Marginal Border Series (MBS) which grew inwards from the vertical walls (Fig. 1a,b). These units follow roughly parallel trends of differentiation into the centre of the intrusion, converging at the Sandwich Horizon (SH). Variations in the textural maturity of basal cumulate rocks indicate that the chamber was filled by several volumetrically minor pulses of magma followed by a last large pulse making the bulk of the magma chamber (Holness *et al.*, 2007b, 2015). After this volumetrically dominant injection of magma, the chamber stayed closed and crystallized.

The stratigraphy of the LS is subdivided, based on changes in the primocryst assemblage, into plagioclase + olivine (Hidden Zone, HZ and Lower Zone a, LZa), plag + ol + augite, ± pigeonite (LZb), plag + ol + aug + Fe-Ti oxides (LZc), plag + aug + ox (+ pig; Middle Zone, MZ), plag + ol + aug + ox (Upper Zone a, UZa), plag + ol + aug + ox + apatite (UZb), plag + ol + aug + ox + ap + ferro-hedenbergite (inverted from β-ferrobustamite; UZc), where plag is plagioclase, ol is olivine, aug is augite, ox is Fe-Ti oxides, pig is pigeonite and ap is apatite (Fig. 1a). The MBS is subdivided in an analogous manner into HZ*, LZa*, LZb*, LZc*, MZ*, UZa* and UZb* (Hoover, 1989), as is the UBS (LZa', LZb', LZc', MZ', UZa', UZb', UZc'; Salmonsen & Tegner 2013). In the three series, continuous fractional crystallization is recorded by the compositions of the primocryst minerals, which change systematically with stratigraphic height (Hoover, 1989; McBirney, 1989; Salmonsen & Tegner, 2013). Bulk-rock incompatible element concentrations suggest that the proportion of solidified interstitial mush liquid is higher in the UBS and MBS (> 30 %) than in corresponding sub-zones of the LS, especially after the appearance of magnetite (< 10 %; Hoover, 1989; Tegner *et al.*, 2009; Salmonsen & Tegner 2013; Namur *et al.*, 2014). The decreasing fraction of interstitial liquid from bottom to top of the LS has been attributed to increasingly efficient compaction of the crystal mush (Tegner *et al.*, 2009), although it could also be ascribed to removal of interstitial liquid by other processes active in the mush such as convection. In a similar way, the higher trapped liquid fraction in the MBS and UBS than in the LS may be attributed to minimal compaction at the vertical walls and roof of the magma chamber (Tegner *et al.*, 2009; Namur *et al.*, 2013; Salmonsen & Tegner, 2013).

SAMPLING AND ANALYTICAL METHODS

Samples used in this study include suites collected during several field seasons and material from drill cores (Fig. 1a; Supplementary Dataset 1; supplementary data are available for downloading at http://www.petrology.oxfordjournals.org). The chosen set of 87 samples covers all stratigraphic units from the LS. A few samples also come from the MBS and were collected from two surface traverses, one on Kramer Island and one on the Skaergaard Peninsula (Fig. 1a). The stratigraphic positions of the samples and the calculated fractions of remaining liquid in the magma chamber are reported in Supplementary Dataset 1. Detailed petrographic description of the samples is given in Tegner *et al.* (2009), Humphreys (2011) and Namur *et al.* (2014).

Plagioclase (Supplementary Dataset 2) and clinopyroxene (Supplementary Dataset 3) major element analyses were performed with a Cameca SX-100 electron microprobe (EPMA) at the University of Cambridge (United Kingdom) and the University of Hannover (Germany). For core compositions, a 15 kV and 15 nA beam was used with a spot size of 5 μm for plagioclase and 1 μm for clinopyroxene. Peak counting times were 20 s for all elements. When possible, at least three points in the core of three grains ($n > 9$) were measured. The values reported here correspond to the mean ($\pm 1\sigma$) of all the measurements that had a total between 98·5 and 101 wt %. For chemical profiles from core to rim we used identical conditions, but the spot size for plagioclase was 1 μm. The following standards were used for Kα X-ray line calibration: diopside for Si and Ca, rutile for Ti, corundum for Al, fayalite for Fe, spessartine for

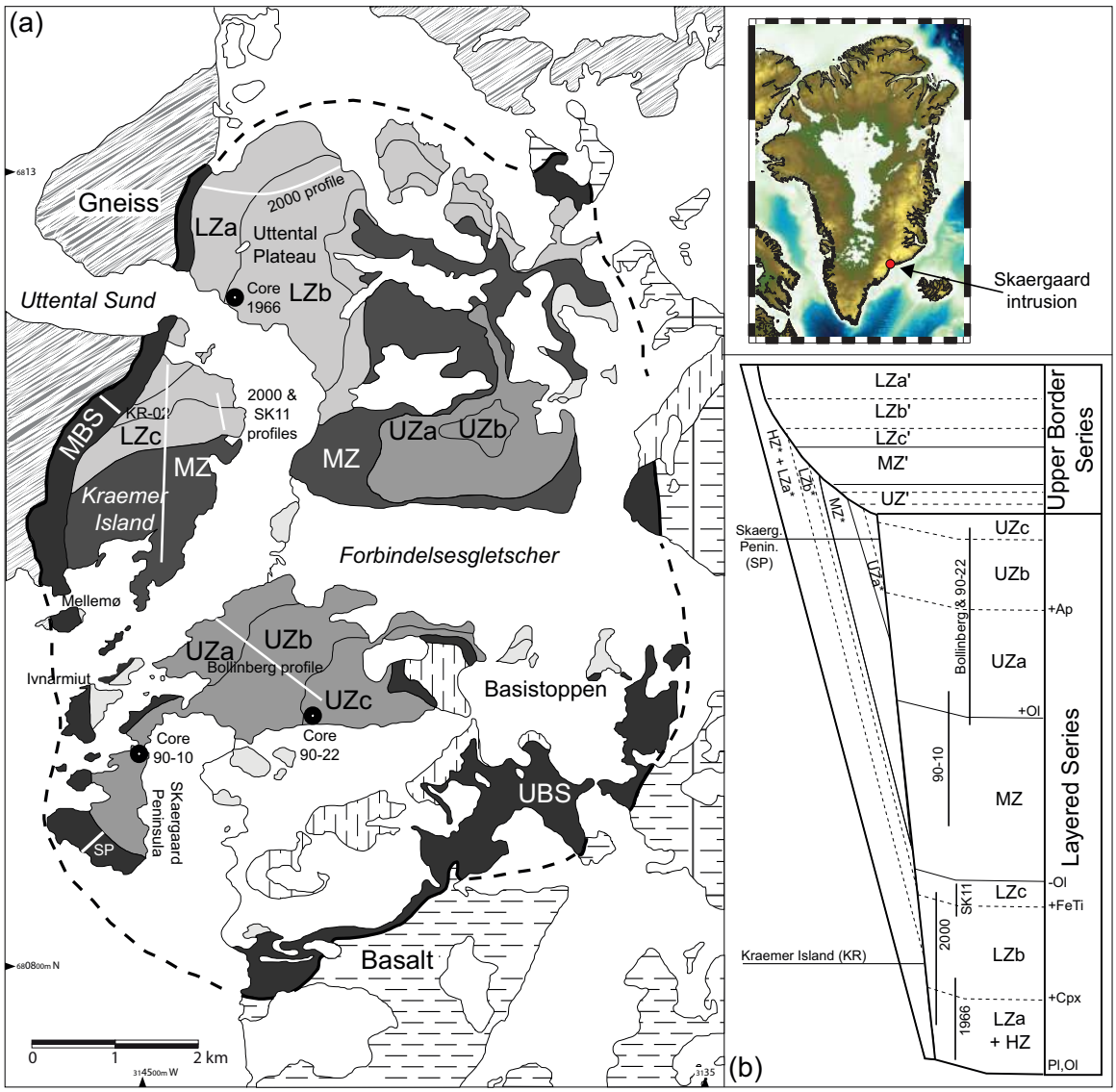

Fig. 1. (a) Simplified map of the Skaergaard intrusion showing the location of the sampling traverses (SP, Skaergaard Peninsula; KR, Kraemer Island, SK-11 and 2000 profile, Bollinberg profile) and drill cores investigated in this study. LZ, Lower Zone; MZ, Middle Zone; UZ, Upper Zone; MBS, Marginal Border Series; UBS, Upper Border Series. Map in the upper right corner shows the location of the map area in Greenland. (b) Schematic cross-section of the Skaergaard intrusion showing the relationships between the LS, UBS and MBS. Subdivisions of each series and the sequence of crystallization in the LS are also shown.

Mn, periclase for Mg, jadeite for Na, K-feldspar for K. Raw data were corrected with the CATZAF software.

In situ trace element analyses of plagioclase (Supplementary Dataset 4) and clinopyroxene (Supplementary Dataset 5) were performed by LA-ICP-MS at the University of Cambridge. A pulsed 213 nm New Wave Research UP213 Nd: YAG laser with 100 mJ energy at a repetition rate of 10 Hz, coupled with an Elan DCR II quadrupole ICP-MS system, was used for ablation. Laser sampling was performed in a He-Ar atmosphere. A beam diameter of 100 μm was used for analyses in the cores (Fig. 2a,b) of the crystals while a beam diameter of 30 μm was used for analyses in rims. The cores of some crystals were too fragile to be analyzed with a large spot (100 μm) and so we measured them with a smaller spot size (10 μm) and performed rastered analyses (Fig. 2c). Analyses were calibrated using ^{29}Si as an internal standard isotope based on SiO_2 concentrations measured by EPMA. During time-resolved analyses of minerals, possible contamination from inclusions and fractures was detected by monitoring several elements (Mg, Si, P, Ca, Ce and Sr) and only the 'clean' part of the signals was integrated. NIST glasses (610 and 612; Pearce *et al.*, 1997) were used as external standards while NIST614, BCR-2 G, BIR-1 G, GOR-128-G (Horn *et al.*, 1997; Norman *et al.*, 1998; Jochum *et al.*, 2005) and in-house standards were used as secondary standards. Precision and accuracy were determined by repeated analyses of NIST, BCR, BIR and GOR glasses and natural samples (for precision). Most trace elements are determined with accuracy better than ±10 % with respect to published values. Elements

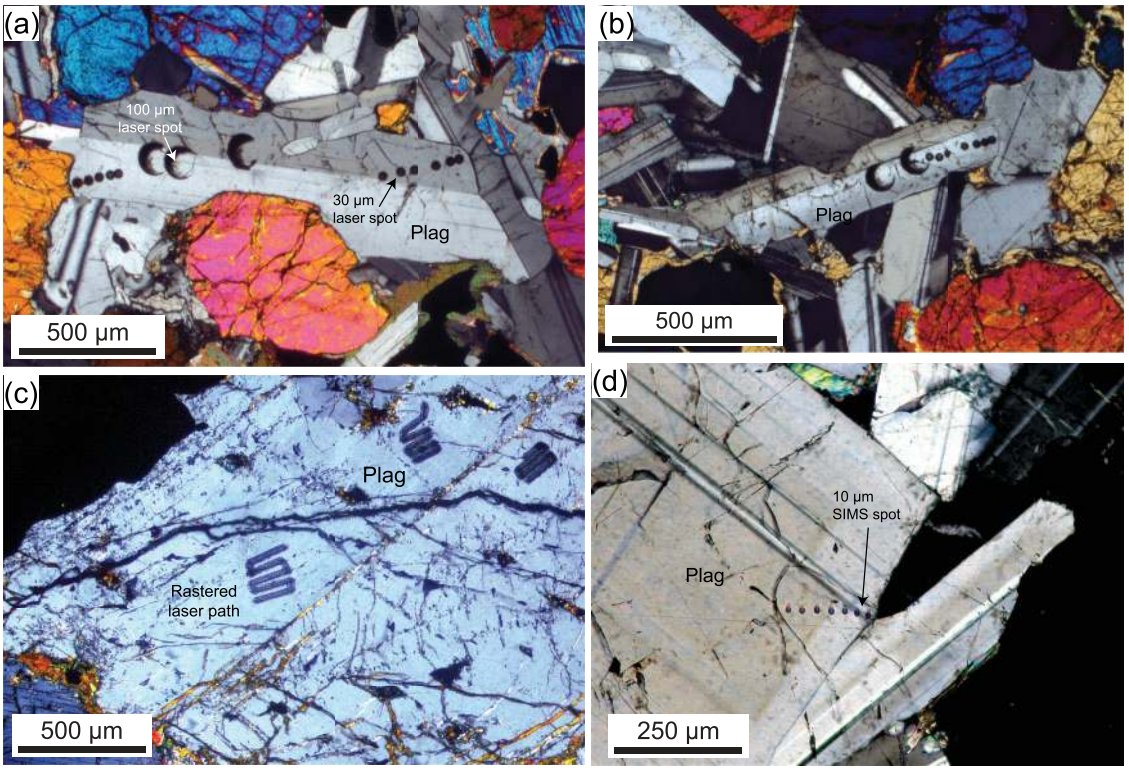

Fig. 2. (a, b) Photomicrographs of sample 458242 (LZa, Layered Series) showing large laser spots (100 μm) in the cores of plagioclase grains and smaller laser spots (30 μm) in plagioclase rims. Transmitted, cross-polarized light. (c) Photomicrograph of sample 84–376 (UZc, Layered Series) showing rastered laser ICP-MS paths in the core of a plagioclase grain. Transmitted, cross-polarized light. (d) Photomicrograph of sample 118678 (LZa, Layered Series) showing ion probe (SIMS) spots in the core and rim of a plagioclase grain. Note the color change between the plagioclase core and the rim Transmitted, cross-polarized light.

with recoveries outside this range were not used in this study. Repeat analyses also indicate a typical 1σ relative precision better than ±5–10 % for all elements (Supplementary Dataset 6). Data were reduced with Glitter 4.0.

In situ plagioclase (Supplementary Dataset 7) and clinopyroxene (Supplementary Dataset 8) trace element analyses of selected samples were also performed by secondary ion mass-spectrometry (SIMS) at the NERC Ion Microprobe Facility in the School of GeoSciences at the University of Edinburgh, UK (Fig. 2d). We used a Cameca ims-4f with a 5 nA primary O^- ion beam, an accelerating potential of 10 kV, a beam current of 5 nA and a secondary accelerating voltage of 4500 V minus a 75 V offset. The beam size was ~ 10 μm in diameter and was not rastered. For plagioclase, the following isotopes were measured for 10 cycles, with counting times in seconds in parentheses: ^{26}Mg(30), ^{30}Si(20), ^{31}P(50), ^{39}K(20), ^{42}Ca(20), ^{49}Ti(50), ^{51}V(50), ^{52}Cr(50), ^{85}Rb(50), ^{88}Sr(50), ^{90}Zr(50), ^{138}Ba(50), ^{139}La(50) and ^{140}Ce(50). For clinopyroxene, the following isotopes were measured for six cycles: ^{23}Na(33), ^{26}Mg(33), ^{27}Al(33), ^{30}Si(33), ^{39}K(50), ^{42}Ca(33), ^{44}Ca(33), ^{45}Sc(83), ^{47}Ti(50), ^{49}Ti(50), ^{51}V(83), ^{52}Cr(83), ^{53}Cr(83), ^{88}Sr(83), ^{89}Y(83), ^{90}Zr(83), ^{139}La(83) and ^{140}Ce(83). Peak positions were verified before each analysis and mass 0·7 was measured to determine background count rates which were sufficiently low to be ignored. Data for ^{51}V and ^{52}Cr were corrected for ^{23}Na^{28}Si interference and ^{23}Na^{29}Si interference, respectively. NIST 610 (Pearce *et al.*, 1997) was used as the calibration standard and concentrations were calculated using JCION-5 software by normalizing intensities to ^{30}Si determined by EPMA. NIST612, NIST614, 95IRV, 95IRW, 95IRX, GSA and GSC were used as external standards (Horn *et al.*, 1997; Pearce *et al.*, 1997; Carpenter *et al.*, 2002). Ion yields determined by analysis of the NIST610 standard showed no systematic drift through the course of the analyses. Correction factors were applied for elements of interest based on comparisons of known ion yields relative to ^{30}Si for plagioclase standards and clinopyroxene standards with those of glass standards (Kovalenko *et al.*, 1988). Precision and accuracy were estimated by repeated analyses of glass and plagioclase standards. Accuracy was found to be better than ±10 % for all elements, except for P (~ 20 %; Supplementary Dataset 9). Typical 1σ relative precision was estimated as ±5–10 % for all elements.

RESULTS

Stratigraphic evolution of mineral compositions

The major element compositions of plagioclase and clinopyroxene in cumulates (troctolites and gabbros; Fig. 3a) from the LS follow trends previously described

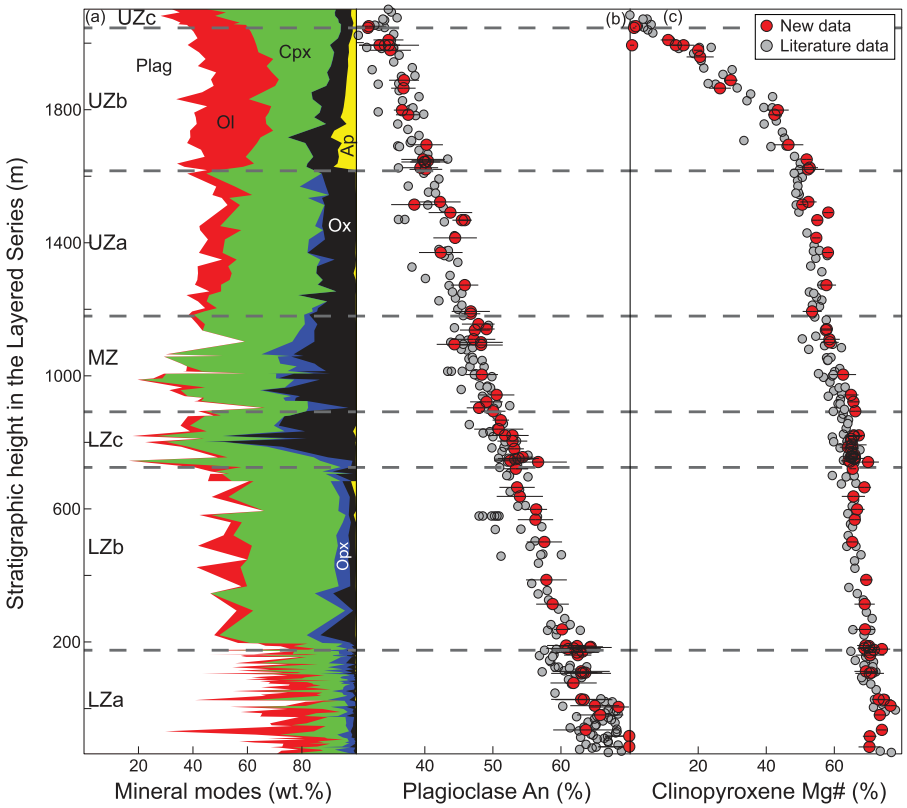

Fig. 3. (a) Stratigraphic evolution of mineral modes in the Layered Series of the Skaergaard intrusion (data from Tegner *et al.*, 2009; Holness *et al.*, 2015). Thick dashed lines represent the boundaries between zones and subzones. Plag, plagioclase, Ol, olivine, Cpx, clinopyroxene, Opx, orthopyroxene, Ox, Fe–Ti oxides, Ap, apatite. (b) Stratigraphic evolution of the An content of plagioclase. Thin horizontal black lines represent 2σ error bars. Red symbols correspond to the samples analyzed in this study. Grey symbols represent literature data (McBirney, 1989; Jang & Naslund, 2001; Toplis *et al.*, 2008; Thy *et al.*, 2009a; Holness *et al.*, 2015). (c) Stratigraphic evolution of the Mg# of clinopyroxene.

in the literature (McBirney, 1989). We observe a continuous and relatively linear decrease of the plagioclase An content [An = Ca/(Ca + Na) mol%; Fig. 3b] with increasing stratigraphic height. The An content decreases from 75 at the bottom of the exposed LS (in the 1966 drill core; Fig. 1b) to 30 in the SH. The clinopyroxene Mg number [Mg# = Mg/(Mg + Fe^{2+}) mol %; Fig. 3c] also decreases continuously from 70 to 0, with the steepest decrease observed in the Upper Zone. Minor elements in plagioclase and clinopyroxene show different trends depending on their degree of compatibility. The TiO_2 content of plagioclase first increases from 0·07 to 0·12 in LZa–LZb before decreasing down to 0·02 from LZc to SH (Fig. 4). A relatively similar trend is observed for TiO_2 in clinopyroxene, although the decrease from LZc to SH is less obvious. Some minor elements in clinopyroxene continuously decrease from bottom to top of the LS (e.g. Al_2O_3 and Na_2O), whereas MnO continuously increases.

Several trends in trace element abundances can be observed. In plagioclase (Fig. 5), Sr, Ba, Eu and other rare earth elements (REE) slightly increase from LZa to UZa and then strongly increase in UZb and UZc. P increases from LZa to UZa before decreasing throughout UZb and UZc, a change which we attribute to the saturation of apatite in the main magma body. We did not observe any element continuously decreasing with stratigraphic height in plagioclase. In clinopyroxene (Fig. 6) Sr, Ba and Eu stay relatively constant or slightly increase from LZa to UZa, before increasing significantly in UZb and UZc. Zr and REE elements (e.g. Ce) decrease from LZa to UZb before they strongly increase in UZc towards SH. Sc increases from LZa to UZb and then decreases in UZc. The decrease in Sc is attributed to the saturation of ferrobustamite ($D_{Sc}^{Cpx/Sil} > 1{\cdot}5$ in ferro-hedenbergite; Dygert *et al.*, 2014; D, partition coefficient; Cpx, clinopyroxene; Sil, silicate melt; Beattie *et al.*, 1993). Co increases from LZa to the top of UZa and then decreases continuously in UZb and UZc. This is presumably related to silicate–sulfide immiscibility (McBirney, 1998; Nielsen *et al.*, 2015) and partitioning of Co into the sulfide melt ($D_{Co}^{Sul/Sil} > 15$; Sul, sulfide melt; Gaetani & Grove, 1997). V increases slightly from LZa to LZc before it decreases strongly and continuously in the Upper Zone as a result of magnetite crystallization (Jang *et al.*, 2001; Toplis & Corgne, 2002). Ni and Cr are the only elements that systematically decrease with stratigraphic height, probably due to their compatible behaviour in olivine, clinopyroxene and Fe–Ti oxides (see D values in Supplementary Material). They are usually below detection limits in UZa–UZc. Both Ni and V concentrations show a spike at ∼ 1100 m These high

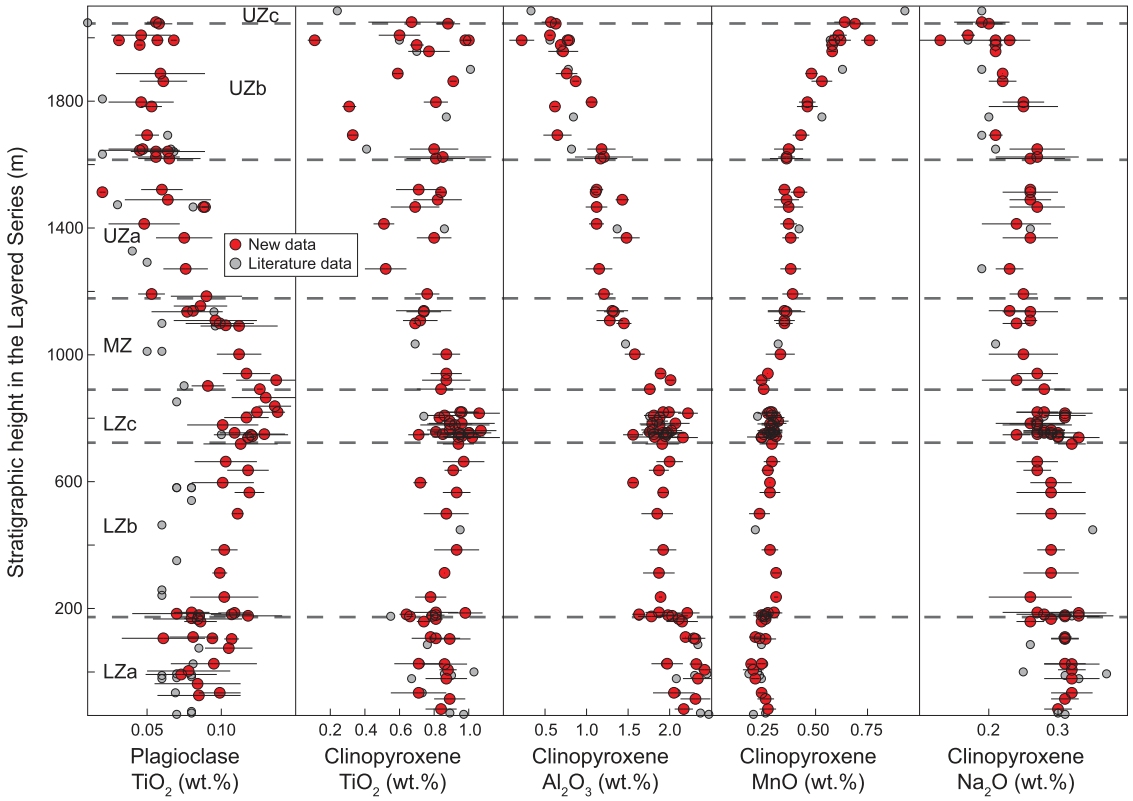

Fig. 4. Stratigraphic evolution of minor elements (EPMA analyses) in plagioclase and clinopyroxene in the Layered Series. Literature data from Jang & Naslund (2001), McBirney (2002), Humphreys (2009) and Holness *et al.* (2015).

values are observed in the 4 samples that we selected in the drill-core 90–10 used in this study (Fig. 1; Supplementary Dataset 1). This may indicate that either mineral compositions are laterally heterogeneous within the LS (90–10 was drilled near the western margin of the intrusion) or that the stratigraphy of the drill core was affected by local faulting.

Chondrite-normalized REE patterns for plagioclase and clinopyroxene are shown in Figure 7. In plagioclase, the heaviest element that can be measured accurately in most samples is Gd. REE in plagioclase are moderately enriched (La: 2–13 times La in CI-chondrite) to slightly depleted (Gd: 0·2–1·2 times Gd in CI). REE patterns are relatively similar throughout the LS, except that the Eu anomaly [Eu/Eu*, with $Eu^* = (Gd_N + Sm_N)/2$] increases from LZ (30 ± 7) to MZ (66 ± 36) and UZ (82 ± 59). No systematic evolution of the degree of fractionation between LREE and heavy rare earth elements (HREE) is observed with increasing stratigraphic height. La/Gd ratios, therefore, stay relatively constant in LZ ($6{\cdot}6 \pm 2{\cdot}3$), MZ ($10{\cdot}1 \pm 3{\cdot}9$) and UZ ($7{\cdot}2 \pm 3{\cdot}3$). In the UZ, REE concentrations are generally higher than those observed in the LZ and MZ. In these samples, elements up to Yb can be measured and we observe an increase in La/Yb ratios from UZa ($4{\cdot}21 \pm 0{\cdot}36$) to UZb ($6{\cdot}56 \pm 3{\cdot}12$) and UZc ($30{\cdot}91 \pm 8{\cdot}88$). This is presumably due to a strong increase in LREE concentrations (Fig. 5).

REE in clinopyroxene are more abundant than in plagioclase (La: 4·1–99 times La in CI; Gd: 16–157 times Gd in CI; Yb: 9–94 times Yb in CI). REE patterns in clinopyroxene show a significant negative Eu anomaly varying from $0{\cdot}55 \pm 0{\cdot}09$ in the LZ to $0{\cdot}67 \pm 0{\cdot}04$ in the MZ and $0{\cdot}73 \pm 0{\cdot}11$ in the UZ. Only a few samples from UZb do not show such a negative anomaly. The degree of fractionation between LREE and HREE decreases with increasing stratigraphic height as illustrated by the decreasing value of the La/Yb ratio from LZ ($1{\cdot}16 \pm 0{\cdot}18$) to MZ ($0{\cdot}82 \pm 0{\cdot}09$) and UZ ($0{\cdot}38 \pm 0{\cdot}29$). In UZ, the total concentration of REE is much higher in UZc than in UZa and UZb.

Core-rim profiles in crystals and rim compositions

We measured a series of compositional profiles and individual points by LA-ICP-MS and by SIMS in zoned plagioclase (Supplementary Data Fig. 1) and clinopyroxene. For the LA-ICP-MS analyses, we used a small laser beam (30 μm) and significant uncertainties are expected for some elements (e.g. Cr, V), whereas the signal/noise ratio was also found to be too small to be used for other elements (e.g. P, HREE). Therefore, we focus only on elements for which errors lower than 10% have been observed for the NIST glasses (i.e. Ti, Sr, Ba, La, Ce, Eu). For SIMS measurements, errors are relatively low (less than 10%) for most elements. For each trace element analysis, we determined the associated major element composition of the crystal by EPMA.

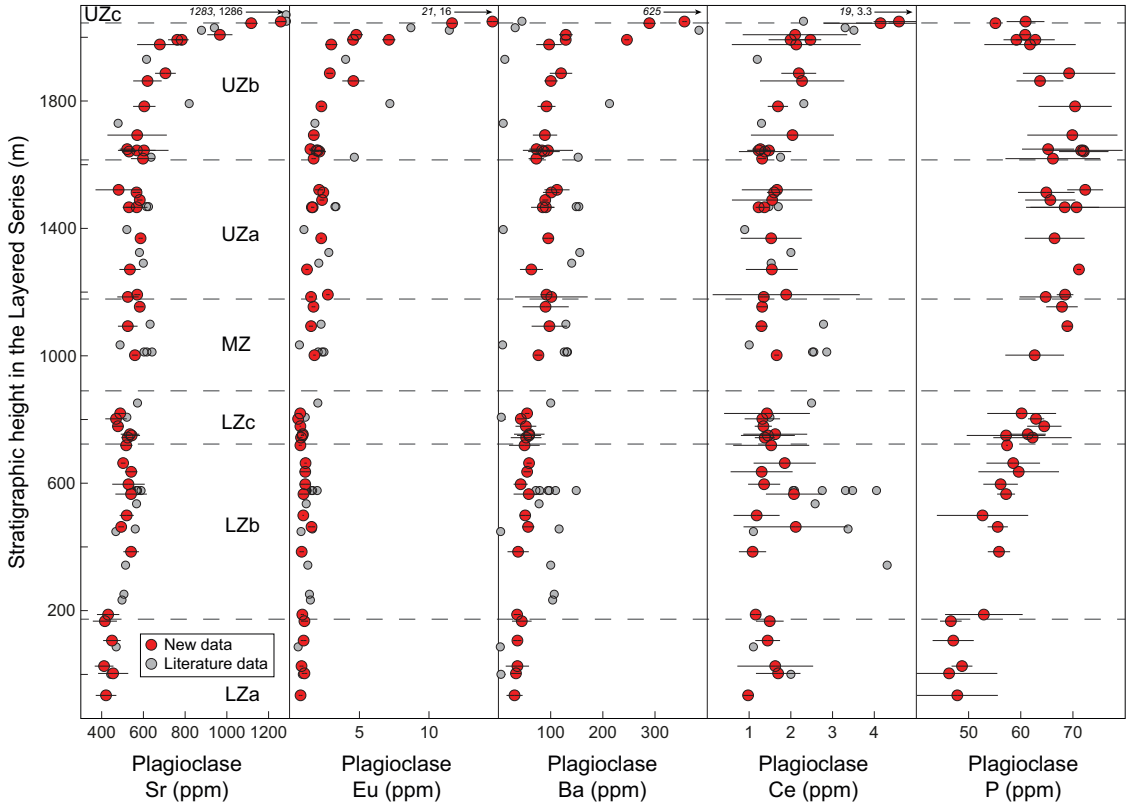

Fig. 5. Stratigraphic evolution of trace elements in plagioclase in the Layered Series. Literature data from Jang & Naslund (2001) and McBirney (2002). Arrows with numbers in the upper part of some panels show the trace element content of bulk plagioclase separates from the Sandwich Horizon (italics; Jang & Naslund, 2001) or core compositions from the Sandwich Horizon (McBirney, 2002). These data are not plotted for scaling purposes. We note that compositions of plagioclase from the SH in Jang & Naslund (2001) and McBirney (2002) are extremely different for some elements and we speculate that mineral separates from Jang & Naslund (2001) may have been contaminated by accessory phases.

In plagioclase, trace element zoning can be observed in almost every crystal that we investigated. However, chemical zoning patterns differ from one element to another and zoning is especially developed in samples from the LZ (particularly LZa and LZb; Fig. 8) and in samples from the UZ (UZa and UZb; Fig. 9). In samples from the LZ and to a lesser extent in samples from the UZ, the An content of plagioclase shows two different patterns described in Namur *et al.* (2014): (1) a core of constant An content surrounded by a rim of decreasing An content (i.e. normal zoning); and (2) a core of constant An content, followed by a mantle of decreasing An content and a rim buffered to a constant composition (An_{55-58} in LZa, An_{49-51} in LZb, An_{39-41} from MZ to UZa). The second type of profile is not observed in rocks from UZb and UZc (Namur *et al.*, 2014). Although the core-rim evolution of An is different in these two types of profiles, the evolution of trace elements is relatively similar (Fig. 8). In detail, we observed very little zoning for Sr or a moderate increase of the Sr content in the rims. In contrast, Ba increases continuously from core to rim. In most samples, even the core of the grains (defined as the internal region with constant An content) shows a progressive increase in Ba towards the rim (Fig. 9). The most impressive zoning patterns are shown by LREE (up to Sm) as represented by Ce in Figure 8. They usually show low and homogeneous concentrations in the core followed by a progressive and continuous increase in the rim. In contrast to other elements such as Sr or Ba, the Ce content in the outermost part of the rim significantly exceeds the highest concentrations observed in plagioclase cores from any stratigraphic interval of the Skaergaard intrusion (<5 ppm; Fig. 10). Jang & Naslund (2001) reported high Ce contents in plagioclase cores from the SH (up to 20 ppm) but, as discussed below, this analysis may have been contaminated by accessory phases. Eu concentration is relatively high in most plagioclase crystals and does not show any obvious zoning or only a slight increase from core to rim (Fig. 10). Ti usually shows flat profiles in plagioclase cores followed by a continuous decrease in the rims. In some crystals from LZa and LZb, Ti shows a bell-shaped profile in the rims where it first increases and then decreases outwards. This behaviour was described using detailed electron microprobe profiles in the LZ (Humphreys, 2009) and was attributed to the saturation of Fe–Ti oxides in the mush liquid. In most profiles that we measured in samples from the LZ, we do not see the initial stage of Ti enrichment and interpret this absence as being due the lower spatial resolution of the LA-ICP-MS compared to the electron microprobe. Relatively similar profiles for all

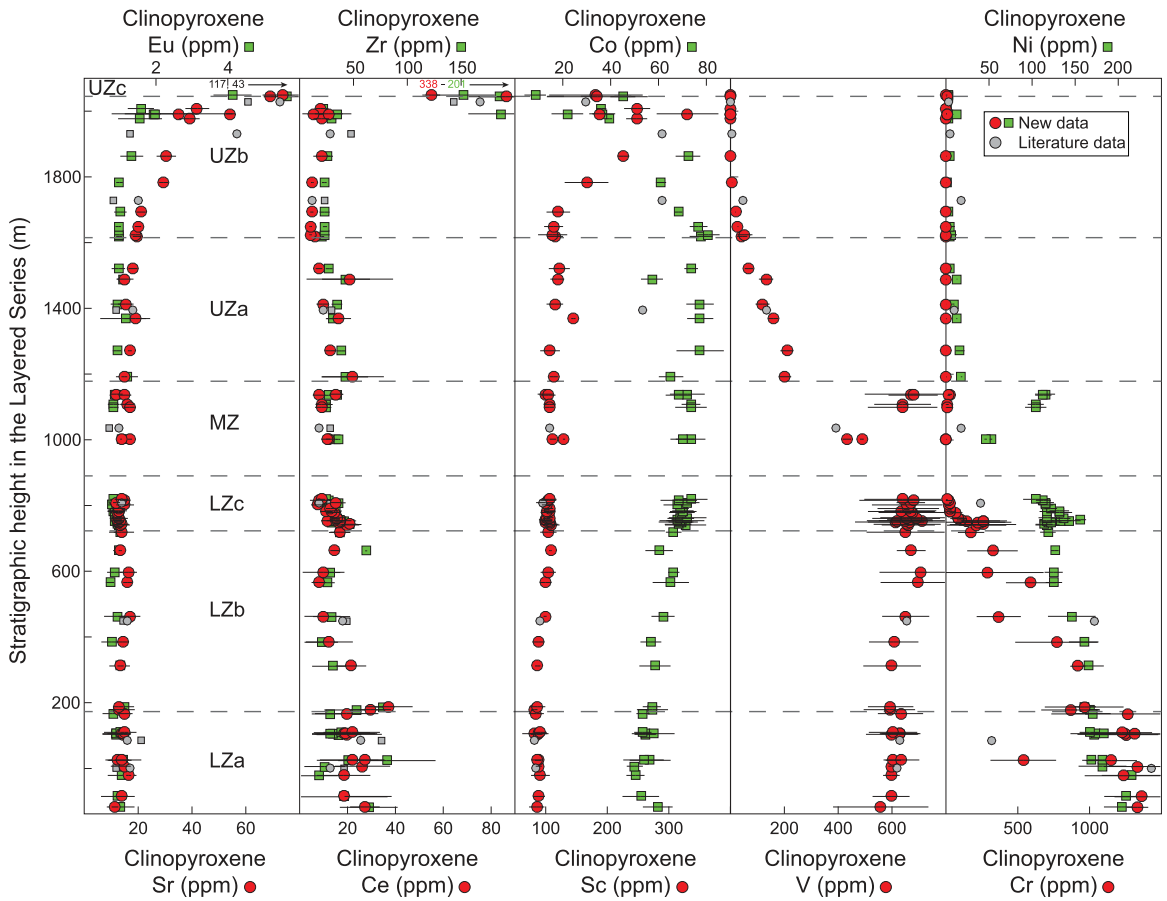

Fig. 6. Stratigraphic evolution of trace elements in clinopyroxene in the Layered Series. Red circles are for Sr, Ce, Sc, V and Cr, whereas green squares are for Eu, Zr, Co and Ni. Literature data are from McBirney (2002).

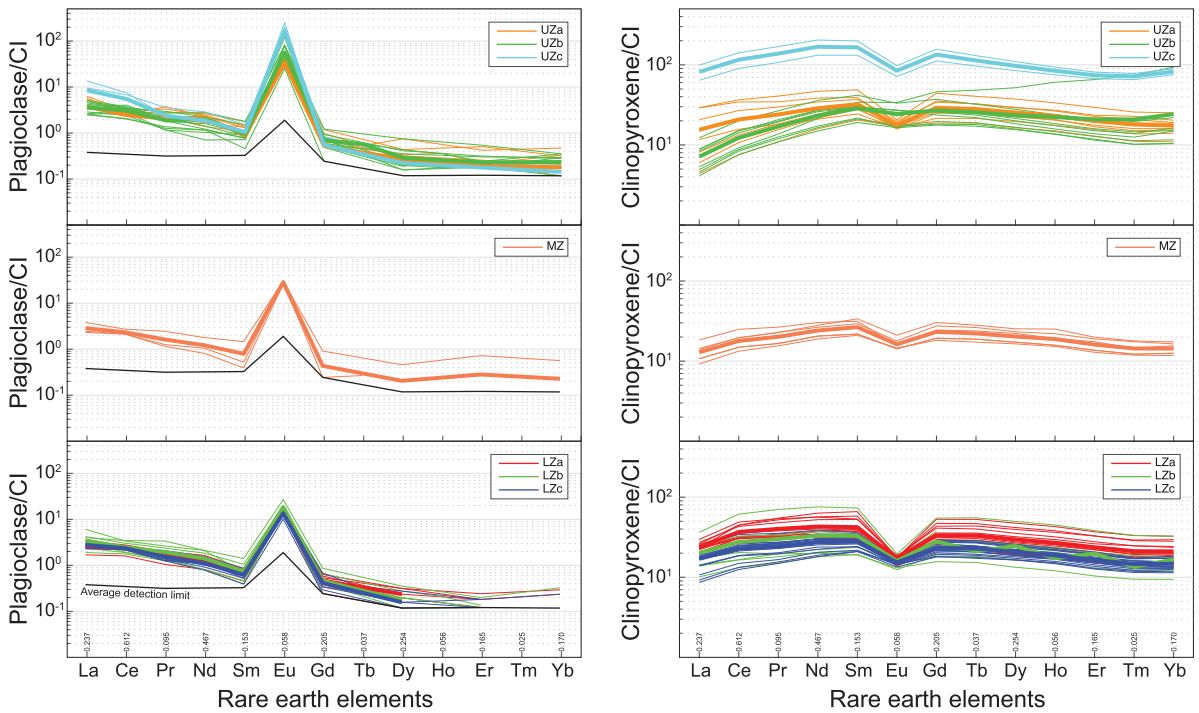

Fig. 7. CI chondrite normalized rare earth element (REE) patterns in plagioclase and clinopyroxene from the Skaergaard LS. Normalization values (Sun & McDonough, 1989) are shown along the base of the plot. Estimated detection limit for LA-ICP-MS analyses is shown in black. Where data for HREE are not shown, this means that concentrations are below the detection limit.

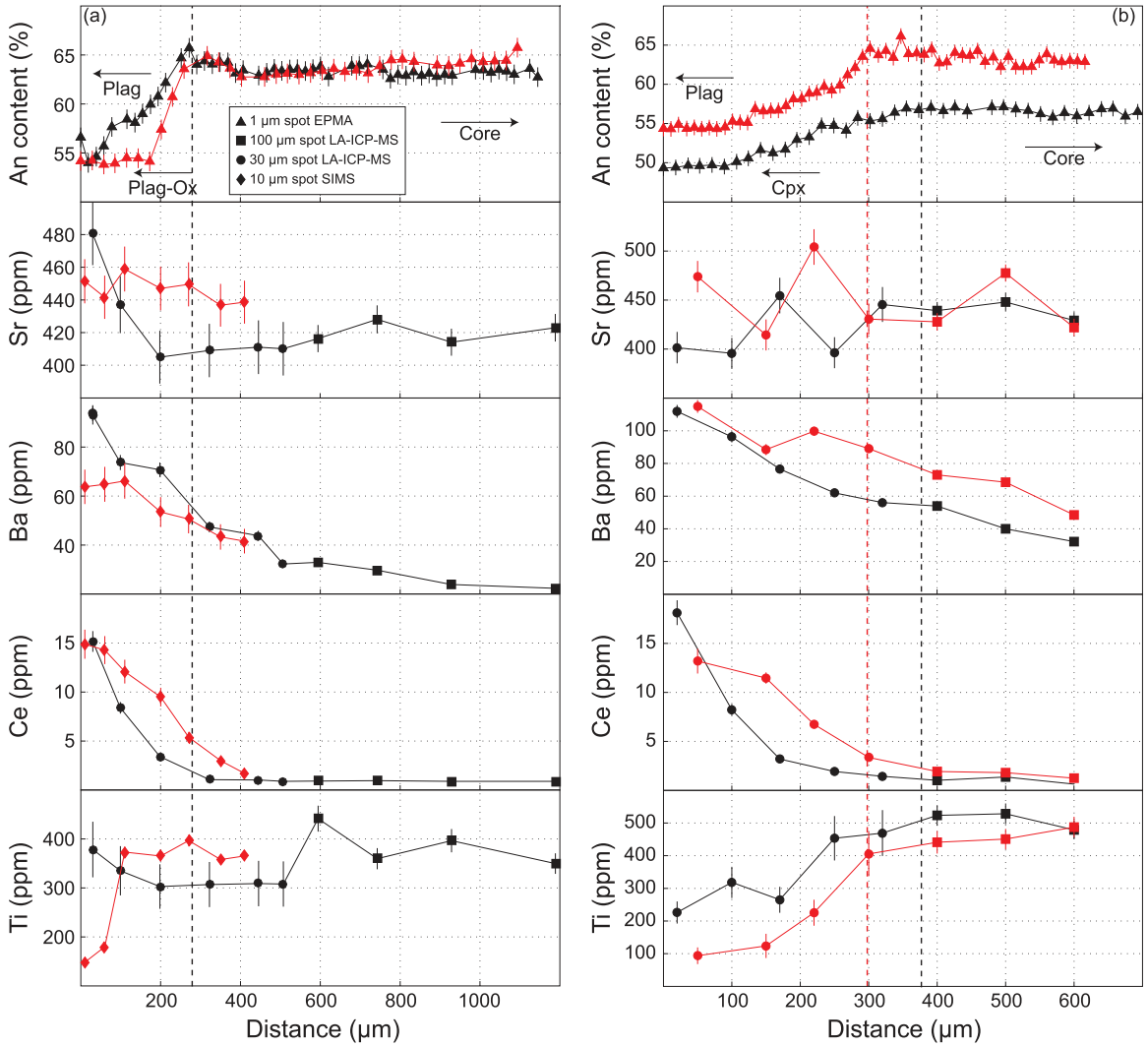

Fig. 8. Major (An content) and trace element profiles in selected plagioclase crystals from the Skaergaard lower zone of the LS. The nature of the phase in contact with the plagioclase is indicated. (a) 118678, LZa (F = 0·78). (b) 458214 (red), LZa (F = 0·71); 458205 (black), LZb (F = 0·46). The error bar for each analysis (LA-ICP-MS or SIMS) was calculated using repeat measurements of plagioclase and glass standards (see Supplementary Datasets 6 and 9). The vertical dashed lines represent the suggested positions of the core–rim boundaries.

trace elements are observed in crystals from the UZ and in the MBS (Fig. 9). However, in a few crystals from the UZ where plagioclase crystals are in contact with granophyric pockets, we observe a decrease of the Ba and Sr contents in the outwards part of the rims. In samples from the UZ and the MBS, we also commonly observe bell-shaped profiles for P (samples measured by SIMS; Fig. 9).

Trace element analyses in clinopyroxene rims were mostly performed by SIMS in a limited number of samples. In HZ–LZa and LZa*, clinopyroxene forms large oikocrysts and relative distances from the core of the crystals cannot be accurately determined. Major elements (Mg#) usually do not show any obvious evolution towards the external part of the grains, whereas minor elements such as TiO_2 and Al_2O_3 decrease (Humphreys, 2009). We observe a large range of trace element concentrations with incompatible elements (e.g. Zr, REE, Y) increasing (outwards) with decreasing TiO_2 and Al_2O_3, while compatible elements (mostly Cr) decrease. From the top of LZa (or LZa*), where clinopyroxene starts to form tabular grains, a more systematic evaluation of zoning profiles is possible. As for the poikilitic clinopyroxene crystals, only minor variation of the Mg# is observed from core to rim. In contrast, a strong increase in incompatible elements and a strong decrease in compatible elements are generally observed (Fig. 11). An important observation for clinopyroxene concerns the behaviour of highly incompatible elements such as REE and Zr (McBirney, 2002). When REE (Ce for LREE and Y as a proxy for HREE) are plotted against Zr, two different trends are observed. Clinopyroxene rims in samples from the LZ have much lower REE contents at a given Zr content than rims in samples from the UZ. Samples from the MZ seem to plot between these two trends (Fig. 12). Such a

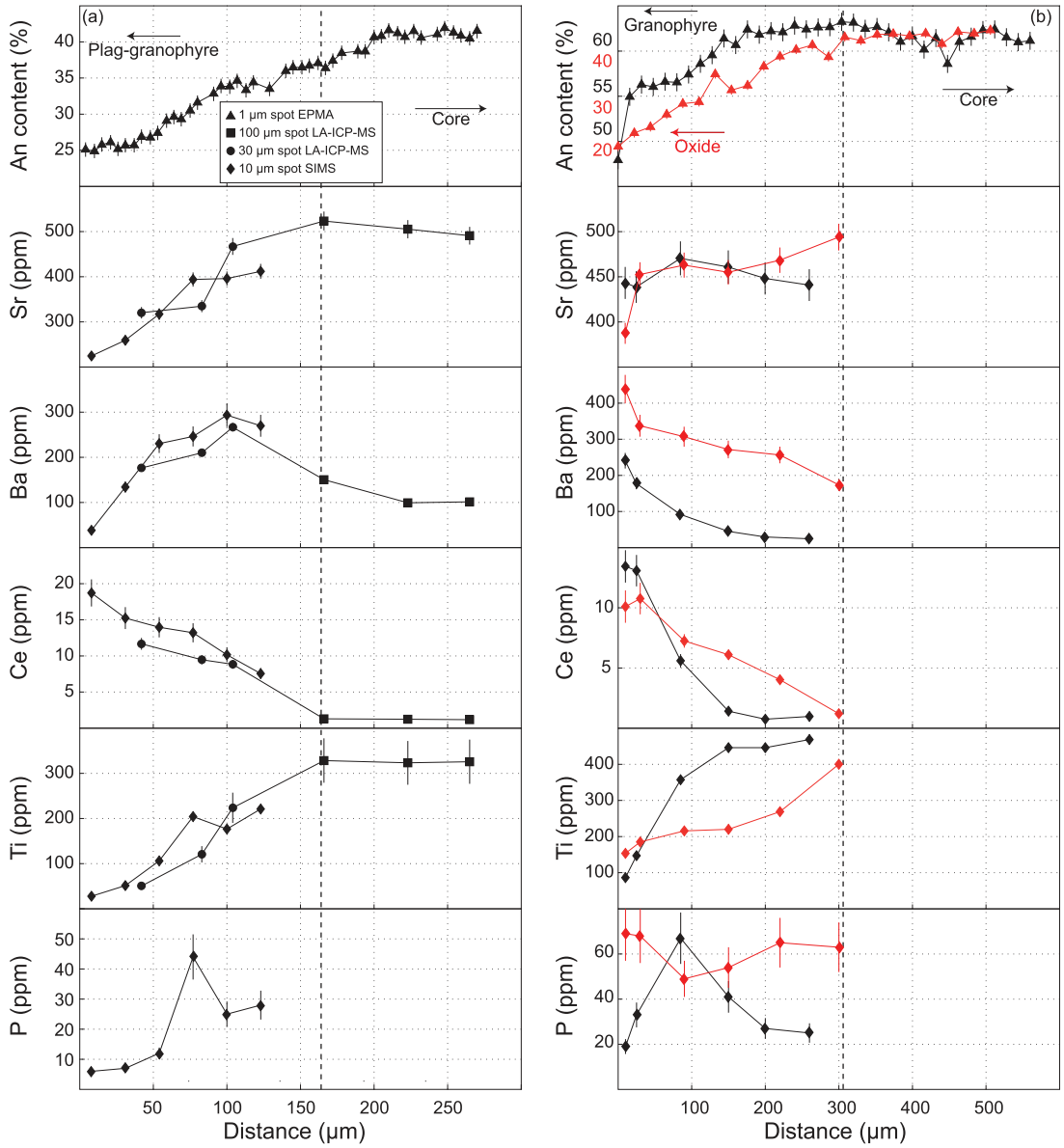

Fig. 9. Major (An content) and trace element profiles in selected plagioclase crystals from the Skaergaard upper zone of the LS and the lower and upper zones of the MBS. (a) 90–22-481·8, UZa (F = 0·10). (b) SP-46 (black), LZa* (or LZb*) (F = 0·68); SP-26 (red), UZa* (F = 0·15). Note the two different Y axes (black and red) for An.

decoupling is not observed in crystal cores for which all compositions plot on a single trend. However, a relatively similar decoupling between 3+ cations and 4+ cations was previously reported for Al^{3+} and Ti^{4+} in clinopyroxene cores (Nwe, 1976). It was attributed to contrasting substitution mechanisms of minor elements in the pyroxene lattice. In agreement with these data, our new analyses of clinopyroxene cores also reveal a higher proportion of Al^{3+} at a given Ti^{4+}content in LZ than in UZ (and MZ; Supplementary Data Fig. 2a). It is, therefore, interesting to note that the behaviour of 3+ (Ce, Y) and 4+ (Zr) trace elements in clinopyroxene rims is opposite to that of 3+ and 4+ major elements (Al^{3+} and Ti^{4+}) in crystal cores. Indeed, we observe lower abundances of 3+ cations (Ce, Y) at a given content of 4+ cations (Zr) in clinopyroxene rims from the LZ than in clinopyroxene rims from the UZ. We also note that there is no link between the incompatible trace element content (Zr and REE) and the concentration of Ti^{4+} or Al^{3+} in the clinopyroxene (Supplementary Data Fig. 2c). This is surprising because REE partition coefficients between plagioclase and clinopyroxene are commonly assumed to be strongly related to the Al and Ti content of the clinopyroxene (Bédard, 2014). This may indicate that the changing behaviour of Zr and Ce in clinopyroxene rims from LZ to US may not be related to a simple change in substitution mechanisms in the pyroxene lattice.

In order to assess and quantify possible re-equilibration and interdiffusion of fast and slow diffusing elements between silicate minerals (Coogan & O'Hara, 2015), we measured the major and trace

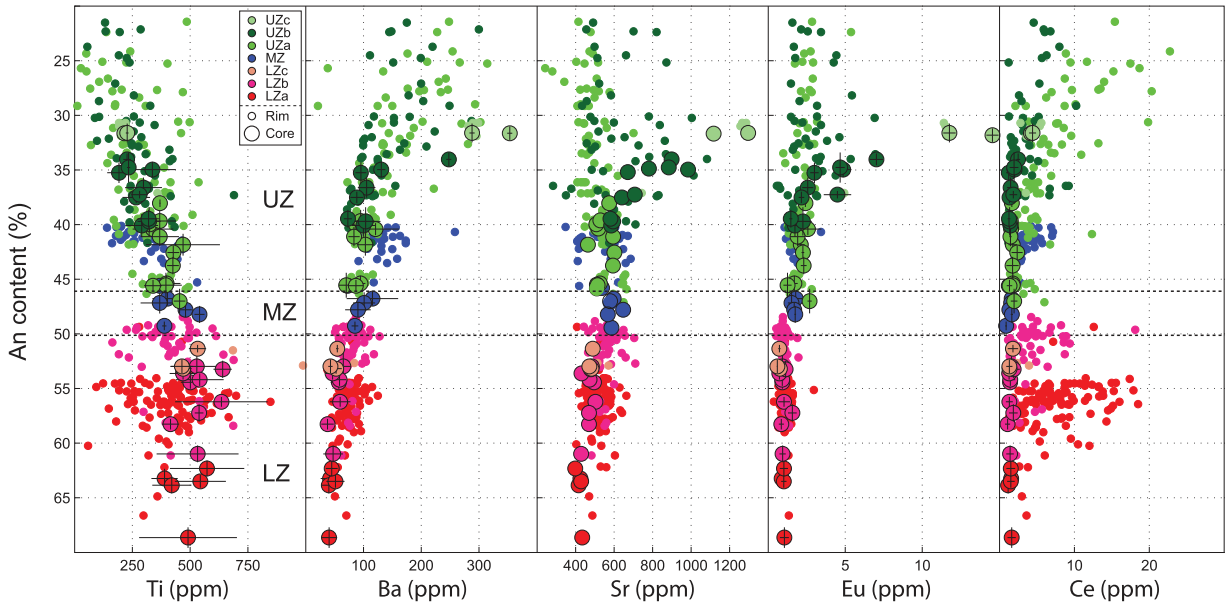

Fig. 10. Evolution of selected trace elements in plagioclase as a function of the plagioclase An content (%). Core and rim compositions are shown as well as the stratigraphic subdivisions of the LS. The An content of plagioclase at the boundary between successive units is based on McBirney (1989) and Namur *et al.* (2014).

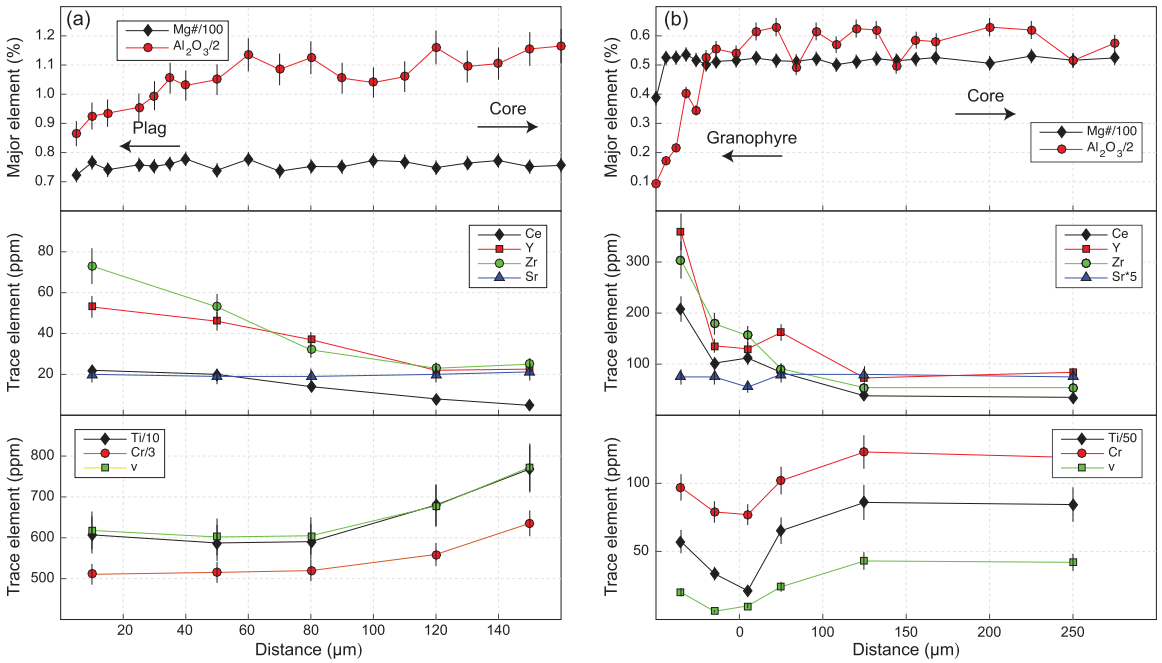

Fig. 11. Major (Mg#), minor (Al_2O_3, TiO_2) and trace element profiles in representative clinopyroxene crystals from the Skaergaard LS and MBS. (a) SP-46, LZa*-LZb* (F = 0·68). (b) 90–22-481·8, UZa (F = 0·10).

element compositions of adjacent plagioclase and clinopyroxene crystals in a single sample (SK84–358; LZc; Fig. 13). Major elements (An content of plagioclase and Mg# of clinopyroxene) and mildly compatible elements (Sr, Ba) show little zoning. Transition metals are low in plagioclase, but continuously decrease (Ni, Cr and V) from core to rim in clinopyroxene. LREE elements (La to Eu) significantly increase in the plagioclase rim while they slightly decrease in the clinopyroxene rim. LREE in the plagioclase rim (up to 5 ppm Ce) however do not reach the extremely high concentrations (Ce > 20 ppm) observed in many other crystals from LZa and LZb (Fig. 10). The absence of such an extreme LREE enrichment in the plagioclase rim reported in Figure 13 may be due to early impingement of plagioclase and clinopyroxene crystals during solidification of the

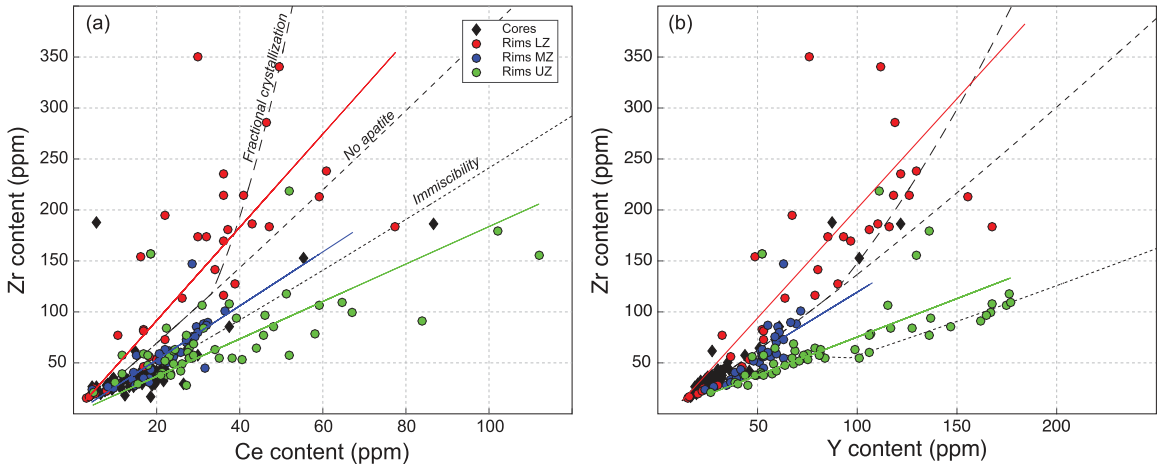

Fig. 12. Evolution of selected trace elements in clinopyroxene cores and rims of the Skaergaard LS and MBS. (a) Zr (ppm) *vs* Ce (ppm). (b) Zr (ppm) *vs* Y (ppm). Colored lines show simple linear regressions for each zone of the intrusion (LZ + LZ*; MZ; UZ + UZ*). Dashed and dotted lines show expected trends from simple fractional crystallization, fractional crystallization without apatite and development of silicate-liquid immiscibility. Fractional crystallization model (with or without apatite) use cotectic proportions from Thy *et al.* (2006). For simplicity we used constant partition coefficients between crystals and melt (i.e. partition coefficients do not evolve with temperature, melt composition or crystal composition). In the model simulating silicate liquid immiscibility, we considered that the immiscibility process started after 80% of fractionation (residual liquid fraction = 0·2). Trace elements are distributed between conjugate immiscible melts according to the partition coefficients from Schmidt *et al.* (2006). See text for details.

liquid in the crystal mush which could have hampered further crystal growth from the most evolved interstitial melts (Holness *et al.*, 2013: Namur *et al.*, 2013). It is also well known that samples from LZc contain much less material crystallized from trapped liquid than samples from LZa and LZb (Tegner *et al.*, 2009; Namur *et al.*, 2014).

DISCUSSION

In the following discussion, we consider a model of a magma chamber in which crystallization occurs in two main regions (Fig. 14): (1) at the interface between a solid + liquid crystal mush and the main magma body. This is where primocrysts (e.g. crystal cores) form. Subsequent crystallization of primocrysts will bury early formed crystals in the solid + liquid crystal mush; (2) in the solid + liquid crystal mush. This is where interstitial phases and crystal overgrowths form. In the first part of the discussion we use geochemical models to investigate the geochemical evolution of the Skaergaard parental magma and the equilibrium minerals forming in the main magma body (i.e. at the interface with the crystal mush) during fractional crystallization. These data are then compared with crystal core compositions measured along the Skaergaard stratigraphic column to evaluate the extent fractional crystallization can explain the geochemical evolution of cumulus phases in Skaergaard. In the second part of the discussion, we investigate the processes that may affect the composition of crystal rims that formed during solidification of the liquid in the crystal mush. In particular, we assess whether or not rim compositions can be explained by simple crystallization of the mush liquid, or if they have been affected by other processes such as the development of silicate–liquid immiscibility or sub-solidus diffusion. For this second part of the discussion, we especially focus on highly incompatible trace elements and Ce in particular.

Evolution of trace elements during the differentiation of the main magma body

Modelling fractional crystallization

Solidification of the Skaergaard intrusion involved highly effective fractional crystallization of the original ferrobasaltic parent magma (Nielsen, 2004). This is illustrated by the continuous evolution of the major element compositions of plagioclase, olivine and clinopyroxene in the LS (McBirney, 1989; Thy *et al.*, 2009a; Namur *et al.*, 2014), the UBS (Naslund, 1984; Salmonsen & Tegner, 2013) and the MBS (Hoover, 1989; Namur *et al.*, 2013). Highly effective fractional crystallization of the parent magma is also supported by strong enrichment factors for most trace elements between cumulus phases at the bottom of the intrusion (LZa for plagioclase and LZb for clinopyroxene) and those at the top of UZc (Figs 5 and 6; Supplementary Data Fig. 3). Only a few compatible elements show negative enrichment factors, which may also be explained by protracted fractional crystallization. In the following, we test if the stratigraphic patterns of important trace elements in plagioclase and clinopyroxene can be adequately reproduced by simple models of fractional crystallization or whether solidification of the magma chamber involved more complicated processes.

Modelling the fractional crystallization process was performed using the Rayleigh equation (see details in the Supplementary Data). It requires us to make realistic assumptions for several parameters: the parental magma composition of the intrusion, instantaneous cotectic proportions of minerals at each step of crystallization, the amount of interstitial liquid that remains

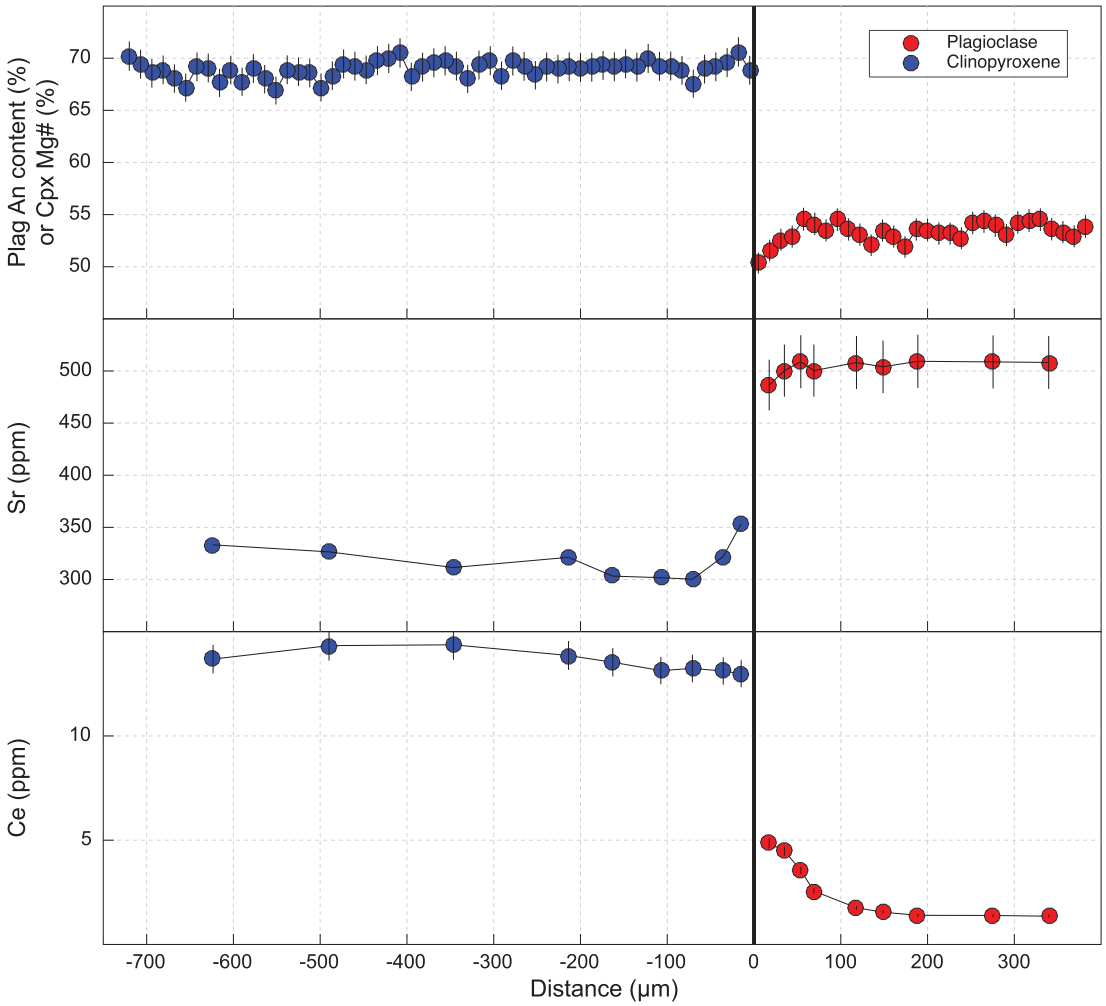

Fig. 13. Major and trace element profiles in adjacent plagioclase and clinopyroxene crystals. The thick vertical black line shows the boundary between the two crystals. SK84–3581, LZc (F = 0·42).

trapped in the cumulate matrix (i.e. does not return to the main magma body and does not contribute to the overall differentiation of the magma chamber, such as *in situ* crystallization; Langmuir, 1989), and mineral-liquid partition coefficients (D) for each element and each phase. As described below, cotectic proportions, trapped liquid fractions and D values are not perfectly constrained. In order to take into account the effect of changing these parameters on calculated liquid compositions, we performed a Monte Carlo simulation with 1000 calculations of fractional crystallization paths. For each simulation, we then calculated the compositions of the equilibrium, liquidus minerals. Details on the parameters and limits used in the calculations are given below, whereas comparison between calculated mineral compositions and those observed in the Skaergaard cumulate rocks are presented subsequently.

A good estimate of the major and trace element composition of the Skaergaard parent magma was proposed by Nielsen (2004) and is used in our models (see Supplementary Data). For elements that were not reported by Nielsen (2004), we complemented our database with the average compositions of East Greenland tholeiitic basalts (Tegner *et al.*, 1998). There is a significant debate about the cotectic proportions of liquidus minerals in the Skaergaard intrusion, especially for Fe–Ti oxides (Toplis & Carroll, 1996; Thy *et al.*, 2009a). This has led to significant discussions about the actual liquid line of descent of the Skaergaard magma (Hunter & Sparks, 1987; McBirney & Naslund, 1990; Toplis & Carroll, 1996; Tegner, 1997; Thy *et al.*, 2009a). In our models, we considered cotectic proportions estimated from equilibrium experiments (Thy *et al.*, 2006) and from mineral modes in cumulate rocks (Fig. 3; Thy *et al.*, 2009a). The effect of using imperfectly constrained cotectic proportions could have a strong effect on modelling results, especially for compatible elements (e.g. Cr, Ni). It could also affect the results for less compatible elements for which mineral/melt partitioning may depend on the major element (e.g. SiO_2) composition of the equilibrium melt (e.g. Dohmen & Blundy, 2014). To take this uncertainty into account, we considered a tolerance of ±5 % relative for the cotectic proportion of each phase given by Thy *et al.* (2006;

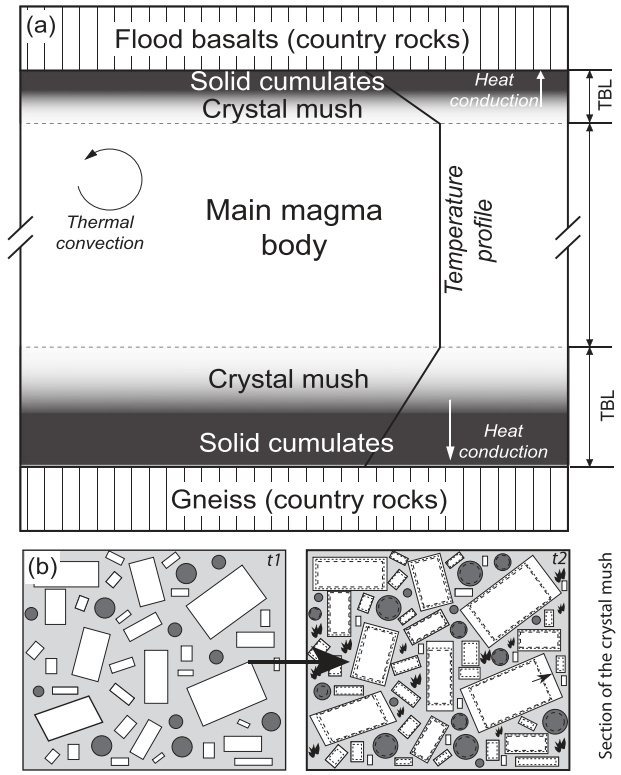

Fig. 14. (a) Schematic model of a magma chamber. The crystal mush forms on the walls, floor and roof of the magma chamber. Modified from Kuritani *et al.* (2007) and Namur *et al.* (2014). We consider that primocrysts that form the cumulate matrix crystallize from the main magma body at the interface between the magma body and the crystal mush. TBL, Thermal boundary layer. (b) Close up of a section of the crystal mush. The mush is made up of crystals and interstitial melt (t1). Solidification of melt produces new interstitial phases and overgrowths (rims) on primocrysts that formed earlier at the interface between the mush and the main magma body (t2). Modified from Namur *et al.* (2014).

see Supplementary Data). Concerning the amount of interstitial liquid in the crystal mush during solidification of the magma chamber, we considered the eventual trapped liquid fractions (e.g. residual porosity) rather than the initial porosity of the mush (Jerram *et al.*, 2003) because convection and/or compaction quickly expel the interstitial melt from the crystal matrix back into the main magma body (Toplis *et al.*, 2008; Tegner *et al.*, 2009; Namur & Charlier, 2012). We estimated trapped liquid fractions using the bulk P_2O_5 contents of cumulate rocks as reported in Tegner *et al.* (2009), Namur *et al.* (2013), Salmonsen & Tegner (2013), Holness *et al.* (2015) and from an unpublished dataset of the MBS available at the University of Cambridge. Calculations were performed using the iterative method described in Namur *et al.* (2014) (see Supplementary Material), except that the actual P content of cumulus plagioclase (Fig. 5) was used in the calculation. This has the consequence of slightly reducing the estimated trapped liquid fraction. Because cumulate rocks form at the floor, roof and walls of the magma chamber at the same time and from the same magma (Salmonsen & Tegner, 2013), the amount of interstitial liquid trapped in cumulates from the three series of the intrusion (LS, MBS, UBS) must be considered in our models. We calculated a weighted average bulk trapped liquid content from the relative volumes of each zone (or subzone) in the LS, MBS and US (Nielsen, 2004; e.g. $X^{IL}_{LZa} \times vol_{LZa} + X^{IL}_{LZa^*} \times vol_{LZa^*} + X^{IL}_{LZa'} \times vol_{LZa'}$; where X^{IL} is the fraction of interstitial liquid and vol. is the volume of each zone (e.g. LZa) in the intrusion). For UZa and UZb (and equivalent subzones in MBS and UBS) where apatite is cumulus, we used trapped liquid fractions calculated from U concentrations for the LS (Tegner *et al.*, 2009). For cumulates in the MBS and UBS for which no U bulk-rock data exist, we considered a residual porosity of 30 %.

For the mineral–liquid partition coefficients (D), we used two different approaches: (1) we compiled an extensive literature dataset of experimentally determined Ds between basaltic melt and minerals present in Skaergaard cumulates (plagioclase: n = 310; n, number of experiments; olivine: n = 75; clinopyroxene: n = 310; magnetite: n = 23; ilmenite: n = 18; apatite: n = 20; the full list of references is given in the Supplementary Data) and used in the Monte Carlo simulations D values within the range of the mean $D \pm 2\sigma$. In these models, D values were kept constant for each simulation of fractional crystallization; (2) we used specific, empirically- or thermodynamically-calibrated, models to calculate adequate D values as a function of temperature, ± crystal composition, ± liquid composition (Blundy & Wood, 1991, 1994; Sun & Liang, 2012; Morse & Allaz, 2013; Bédard, 2014; Dohmen & Blundy, 2014; Dygert *et al.*, 2014). In that case, D values continuously changed in each fractional crystallization model as a function of temperature (Thy *et al.*, 2009b), mineral compositions (e.g. Namur *et al.*, 2012b) and liquid composition (e.g. Nielsen *et al.*, 2009). Fractional crystallization models were performed for a range of residual liquid fractions (F) ranging from 1·0 to 0·005 with an incremental step of 0·01 (1 %; see details in the Supplementary Data).

Modelling results and comparison with Skaergaard minerals

Only a few elements (Ni, Cr) are highly compatible in Skaergaard cumulates (bulk partition coefficients; $\bar{D} > 1$) with concentrations continuously decreasing from bottom to top of the LS. The behaviour of these elements and their concentrations in minerals can be adequately reproduced by a simple model of fractional crystallization of the Skaergaard magma. Cr and Ni show a slow continuous decrease in LZa and LZb due to fractionation of olivine ± clinopyroxene (Hart & Davis, 1978; Toplis & Corgne, 2002), followed by a rapid decrease after the appearance of Fe–Ti oxide minerals, interpreted as resulting from incorporation of both elements into magnetite (Toplis & Corgne, 2002; Fig. 15). V and Co are also compatible, especially in the upper part of the LS. Modelling of V during fractional crystallization is hampered by the lack of accurate constraints on the

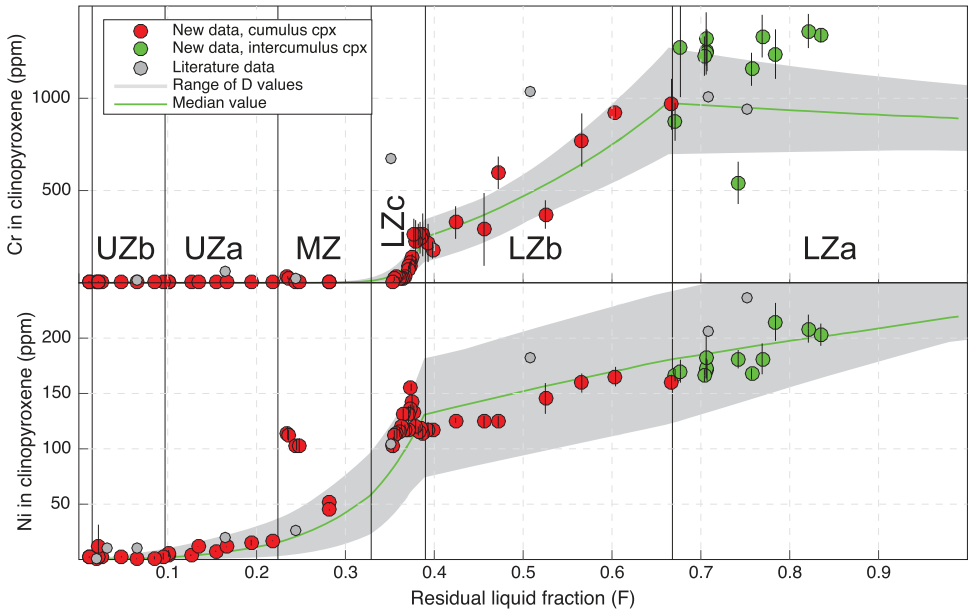

Fig. 15. Models of fractional crystallization (modelled with the Rayleigh equation; see text and Supplementary Data for details) of the main magma body of the Skaergaard intrusion, showing the evolution of compatible trace elements in clinopyroxene as a function of the liquid fraction in the magma chamber (F). Stratigraphic subdivisions of the LS are shown for reference. Modelled clinopyroxene compositions are obtained by inversion of liquid compositions using relevant partition coefficients. The grey fields represent the results of 1000 Monte Carlo simulations performed using D values within the range of average $\pm$ 2 σ of $>$ 300 partition coefficients compiled from the literature. The green trend represents the median value of the data obtained through the Monte Carlo simulation. Symbols represent LA-ICP-MS data of average clinopyroxene cores. Green symbols represent intercumulus crystals, whereas red symbols represent cumulus crystals.

evolution of oxygen fugacity after Fe–Ti oxide saturation and the exact cotectic proportions of magnetite and ilmenite (Toplis & Carroll, 1996; Thy *et al.*, 2009a). However, the strong decrease of V in MZ and UZ together with the strong effect of fO_2 on $D_V^{Cpx/Sil}$ perhaps suggests that Skaergaard magma became more reduced after magnetite saturation (Toplis & Corgne, 2002). We did not attempt to model the behaviour of Co during fractional crystallization due to the absence of agreement on the exact timing on the onset of silicate–sulfide immiscibility, the exact composition and proportion of the equilibrium sulfide phase (Nielsen *et al.*, 2015; Keays & Tegner, 2016) and the large range of experimentally-determined $D_{Co}^{Sul/Sil}$ values (15–200; Gaetani & Grove, 1997).

The vast majority of incompatible trace elements that we measured in plagioclase and clinopyroxene are enriched in evolved cumulates at the top of the LS compared to cumulates at the bottom of the LS (Figs 5 and 6; Supplementary Data Fig. 3). If their evolution is controlled by fractional crystallization, then the bulk D ($\bar{D}$) must be lower than 1. $\bar{D} < 1$ can result either from the specific element being incompatible in all cumulus phases (e.g. Zr), or the element being compatible in one or several phases, but being strongly incompatible in other, major, cumulus phases (e.g. La). In Figure 16, we model the behaviour of some of these elements. Measured concentrations of Sr in plagioclase and clinopyroxene show a slight enrichment from LZa to UZa before strongly increasing throughout UZb and UZc. This pattern is entirely reproduced within the range of Monte Carlo solutions that we obtained using experimental Ds between melt and the different cumulus phases. However, when specific models for $D_{Sr}^{Plag/Melt}$ are applied (Blundy & Wood, 1991; Bindeman *et al.*, 1998; Bédard, 2006; Morse & Allaz, 2013; Dohmen & Blundy, 2014), a decrease in the Sr content of plagioclase and clinopyroxene is expected in the UZ. Empirical models from Bindeman *et al.* (1888), Bédard (2006) and Morse & Allaz (2013) take into account plagioclase compositon (An content) $\pm$ temperature. Thermodynamic models from Blundy & Wood (1991) and Dohmen & Blundy (2014) take into account both the evolution of temperature and plagioclase composition during differentiation (see Supplementary Data). In our models, temperature evolves from 1170°C at F = 1 (F, residual liquid fraction in the magma chamber) to 1023°C at F = 0·01, whereas the An content of plagioclase evolves from An_{70} to An_{30}. Calculated plagioclase major element compositions are in agreement with the mineral compositions observed in the LS (Fig. 3) and the calculated temperatures agree with those reported by Thy *et al.* (2009b). Over this interval of crystallization, $D_{Sr}^{Plag/Melt}$ is expected to evolve from 1·96 to 5·49 using the model of Blundy & Wood (1991) and from 1·66 to 3·78 with the model of Dohmen & Blundy (2014), explaining the predicted decrease of plagioclase and clinopyroxene Sr content in UZa–UZc. In Skaergaard minerals, we do not observe such a decrease. This may indicate that: (1) the actual cotectic proportion of plagioclase in the UZ is lower than expected

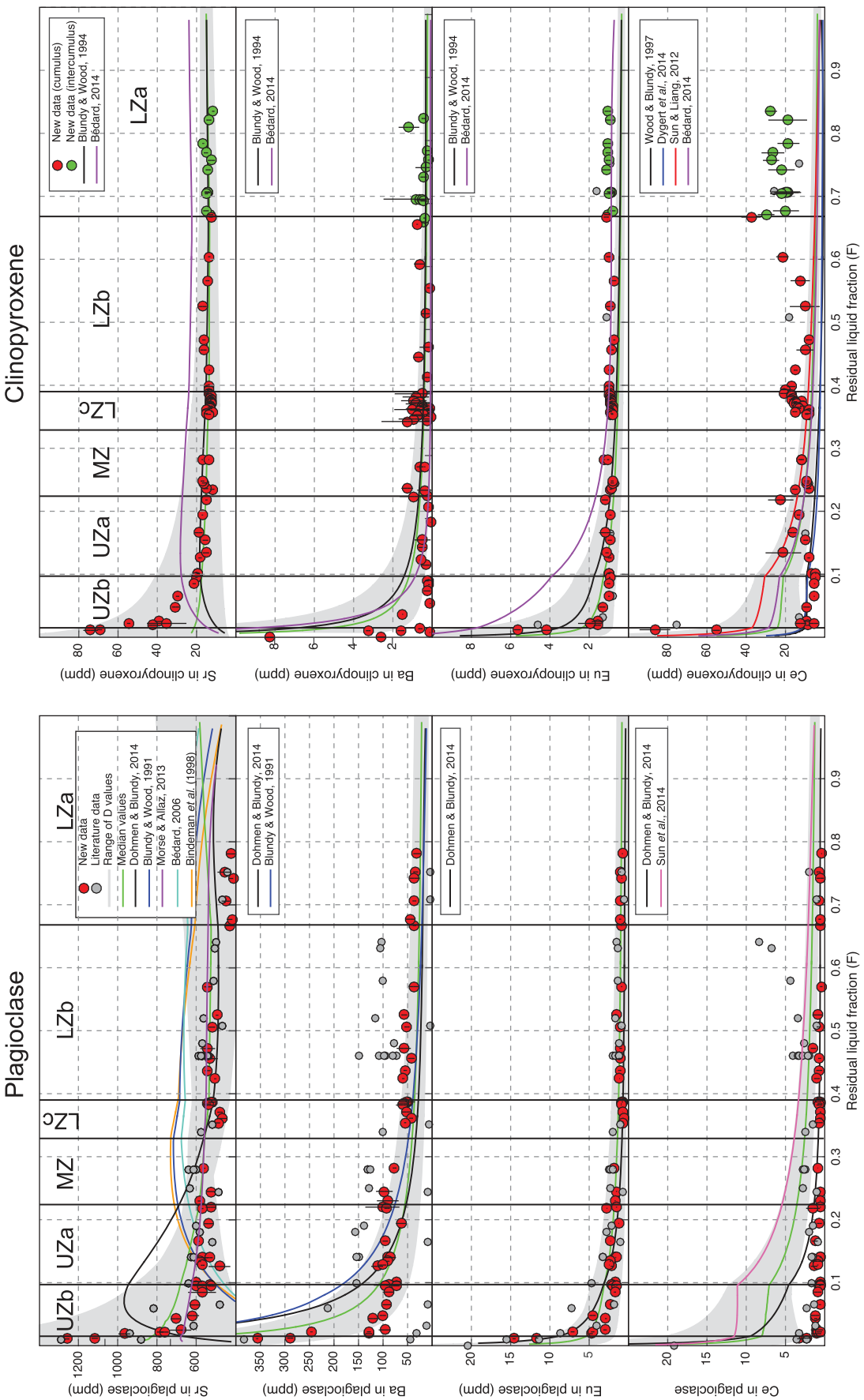

Fig. 16. Models of fractional crystallization of the main magma body of the Skaergaard intrusion showing the evolution of mildly compatible and incompatible trace elements in plagioclase and clinopyroxene cores. The methodology of calculation is identical to that described in Figure 15. Symbols and grey fields are as in Figure 15. Specific models predicting partition coefficients for Sr, Ba and REE were also used and compared with the results of the Monte Carlo simulations. See additional models for Zr and Y in Supplementary Data Figure 6.

from the mineral modes observed in UZ rocks (~ 45%; Tegner *et al.*, 2009; Holness, 2015). In that case, cumulate rocks from UZ would have an excess of plagioclase; (2) thermodynamic and empirical models overestimate $D_{Sr}^{Plag/Melt}$ for evolved plagioclase (e.g. An_{40-30}). This may be due to the low number of experiments performed at low magmatic temperature (~ 1000°C) and involving low-An plagioclase (~ An_{30}; Bindeman & Davis, 2000). The highly variable $D_{Sr}^{Plag/Melt}$ values obtained from experiments and natural glass-phenocrysts pairs in assemblages containing plagioclase $< An_{40}$ may indeed lead to inaccurate prediction of $D_{Sr}^{Plag/Melt}$ for low An plagioclase (Bédard, 2006). However, the absence of a decrease in plagioclase Sr concentrations in the UZ of Skaergaard could also indicate that fractional crystallization became less effective in the upper part of the intrusion where the texture of the rocks changes from typical gabbroic rocks with well-developed lamination to dolerite-like, coarse-grained gabbros containing abundant granophyric pockets (Holness, 2015). The texture of the rocks as well as the deviation between plagioclase and clinopyroxene compositions and the results of fractional crystallization models possibly suggest that, in this part of the intrusion, solidification may dominantly result from equilibrium crystallization at the top of the crystal mush (Nielsen *et al.*, 2015).

Ba and Eu in plagioclase and to a lesser extent in clinopyroxene cores show a progressive increase from the bottom to the top of the LS with a strong increase in UZb and UZc. This evolution can broadly be reproduced by fractional crystallization models using experimental partition coefficients and with specific models of D between plagioclase and melt or clinopyroxene and melt (Blundy & Wood, 1991, 1994; Dohmen & Blundy, 2014). The Eu contents of interstitial clinopyroxene in LZa may, however, be slightly higher than predicted by theoretical models (Fig. 16b). In addition, we observe that the Ba content of plagioclase (and to a lesser extent clinopyroxene) is in the lower range of predicted values in UZa and UZb. The increase in Ba that we see in Skaergaard minerals is, therefore, less pronounced than predicted by fractional crystallization models. Due to imperfectly constrained partition coefficients between the Skaergaard magma and minerals, a fully consistent model of end-member equilibrium crystallization cannot be calculated at low residual liquid fractions ($F < 0{\cdot}2$). However, we observe that a very good fit to the measured plagioclase and clinopyroxene compositions in UZ is obtained by Rayleigh fractionation when the amount of trapped liquid in the crystal mush of UZ is increased. The best fit is obtained with ~ 60% of trapped liquid (Supplementary Data Fig. 4). This confirms that crystallization in the UZ became dominated by equilibrium crystallization because crystals and melt cannot be easily physically separated from each other (Nielsen *et al.*, 2015). The amount of trapped liquid needed to fit the plagioclase and clinopyroxene data is furthermore similar to the initial porosity of a gabbroic mush (Jerram *et al.*, 2003) indicating that very little liquid returns to the main magma body after the formation of the crystal matrix.

Ce evolution is typical of the LREE behaviour. HREE are generally below detection limit in plagioclase. Therefore, we did not model their evolution during fractional crystallization. Ce in plagioclase is very low and constant from LZa to UZb before strongly increasing in UZc. Ce in clinopyroxene progressively decreases from LZa to LZc, is then relatively constant throughout MZ, UZa and UZb before strongly increasing in UZc. The behavior of Ce in both plagioclase and clinopyroxene cannot be accurately reproduced by a model of fractional crystallization, particularly in UZa and UZb. The Ce content observed in plagioclase is systematically too low compared to predictive models, whereas none of the models that we used can reproduce the high Ce contents in clinopyroxene from LZa–LZb. The equations that we used to calculate D values take into account the major element chemistry of the clinopyroxene (e.g. Al, Fe^{2+} and Fe^{3+} on sites M1 and M2; see Supplementary Data) and predict a slightly decreasing $D_{Ce}^{Cpx/Melt}$ (0·22–0·12) with stratigraphic height. However, such a decrease is not sufficient to explain the decreasing Ce content that we observe throughout the LZ. As already pointed out by McBirney (2002), plagioclase and clinopyroxene cores, especially in the LZ, seem to be in chemical disequilibrium for LREE. This can be illustrated by calculated values of $D_{Ce}^{Cpx/Plag}$ which are much higher in Skaergaard cumulates (1–35), than in cumulate rocks from other layered intrusions (Sept Iles, Bushveld, Bjerkreim Sokndal, Kiglapait), oceanic gabbros, extraterrestrial cumulates (eucrites and lunar anorthosites), ferrobasaltic lavas (Iceland, Hawaii) and experimental charges (1–7; Supplementary Data Fig. 5). A likely explanation for such a disequilibrium, especially in LZa, is that clinopyroxene crystallized from the interstitial melt and that poikilitic crystals were continuously re-equilibrated with late-stage, evolved, liquid. A similar model has recently been proposed by Cawthorn & Tegner (2017). Alternatively, fast growth of such crystals may also prevent them from attaining equilibrium compositions, leading to REE uptake in crystal rims (Holycross & Watson, 2016). A more intriguing result of our fractional crystallization models concerns Ce concentrations in UZa–UZb, with predicted values being much higher than the concentrations measured in crystals. In agreement with previous discussion on Sr and Ba, this indicates that solidification predominantly results from equilibrium crystallization in the UZ where the magma chamber was almost fully solid. As for Ba, a much better fit of the data can be obtained with a high trapped liquid fraction (~ 60%) in UZa–UZc, because increasing the trapped liquid fraction drives bulk partition coefficients closer to unity (Supplementary Data Fig. 4). Such a trapped liquid fraction is much higher than what can be estimated from bulk-rock incompatible trace element concentrations (< 20%; Tegner *et al.*, 2009). This discrepancy probably

results from the use of incorrect estimates of liquid compositions in the calculations of trapped liquid fraction. It is now recognized that silicate liquid immiscibility played an important role in Skaergaard, particularly during the solidification of the crystal mush (Holness *et al.*, 2011, 2017; Humphreys, 2011; Nielsen *et al.*, 2015). The development of silicate liquid immiscibility may drastically affect the composition of the liquid in the crystal mush due to density-driven segregation of conjugate immiscible melts (Holness *et al.*, 2011; Namur *et al.*, 2015). Real trapped liquid fractions in cumulate rocks may, therefore, significantly deviate from those calculated when silicate liquid immiscibility is not taken into account (Tegner *et al.*, 2009). It should also be emphasized that the evolution of LREE in the UZ may also be affected by the crystallization of apatite for which actual cotectic proportions are poorly known and for which little data on liquid–crystal D values exist (Watson & Green, 1981; Fujimaki, 1986; Prowatke & Klemme, 2006). However, Zr and Y concentrations in clinopyroxene cores in UZa–UZb are also lower than expected from fractional crystallization models (Supplementary Data Fig. 6). These two elements are less compatible (Y) or incompatible (Zr) in apatite, suggesting that this is not an important consideration.

Fractional crystallization in the main magma body: summary

The results of our models indicate that the evolution of compatible and incompatible elements in crystal cores of the Skaergaard intrusion can be broadly reproduced within the context of fractional crystallization, except in the UZ. The use of trace elements as opposed to major elements gives a more detailed view of the fractionation process and allows a better understanding of the role of individual phases (e.g. Fe–Ti oxides, olivine, plagioclase, apatite) on the behaviour of trace elements (e.g. Cr, Ni, Sr. REE). Major elements in cumulus phases (e.g. An content of plagioclase, Mg# of clinopyroxene) evolve almost linearly from the base to the top of the intrusion (except in UZb–UZc for Mg#) and their evolution is, therefore, relatively insensitive to minor changes of mineral assemblages and cotectic proportions, but can be affected by re-equilibration with trapped liquid (Barnes, 1986; Bédard *et al.*, 2007). In contrast, trace elements can be used to decipher the efficiency of the fractional crystallization process during the solidification of the Skaergaard magma chamber. In particular, the evolution of all elements in UZa–UZc departs from geochemical trends expected from fractional crystallization, suggesting that this process becomes less effective during the last stages of crystallization. It is then replaced by a higher proportion of *in situ* equilibrium crystallization. Although it is known that cumulate layers may form from very thin, metre-scale, magma bodies (Bédard, 2015), we believe that the higher proportion of *in situ* equilibrium crystallization in the UZ may result from the magma chamber being almost solid at this stage of crystallization, leaving little free space for a magma body between the crystal mush sections forming on the floor, roof and wall of the magma chamber. Therefore, this may hamper efficient separation of residual melt and crystals, which is necessary for fractional crystallization. In addition, the low temperature and very high viscosity of the residual melts ($\log \eta = 5{\cdot}8$ Pa s at 1000°C using the viscosity model of Giordano *et al.* (2008) and the melt composition of Nielsen *et al.*, 2009) may also contribute to significant reduction of the efficiency of crystal–melt segregation at low residual liquid fractions. Silicate liquid immiscibility is also known to develop in the UZ of the Skaergaard intrusion (Jakobsen *et al.*, 2005, 2011). This process is however unlikely to exert any control on the trace element distribution in cumulus phases (core compositions) because both melts stay in equilibrium at the top of the mush and crystallize the same phases in different proportions (Charlier *et al.*, 2011; Namur *et al.*, 2012a). Therefore we believe that immiscibility in the main magma body cannot explain the mismatch between measured plagioclase and clinopyroxene compositions and the results of fractional crystallization models (Fig. 16).

Evolution of trace elements in the crystal mush

It is commonly assumed that differentiation of the mush liquid follows a trend similar to that of the main magma body (Coogan *et al.*, 2000a,b; Meurer & Claeson, 2002; Lissenberg *et al.*, 2013; Coogan & O'Hara, 2015). For the Skaergaard intrusion, differentiation of the mush liquid was shown by the evolution of Ti concentration in core–rim profiles in plagioclase crystals (Humphreys, 2009, 2011). However, the use of mineral compositions to track melt differentiation relies on the assumption that elements are immobile after they have been entrapped in the crystal lattice during crystal growth. Although this may be the case for Ti in plagioclase, other, faster diffusing, elements can experience strong diffusive re-equilibration after crystal growth (Barnes, 1986; Coogan & O'Hara, 2015). In addition, other processes such as infiltration metasomatism, replenishment or migration of interstitial melt, fluid flow or dissolution–reprecipitation could disrupt the chemical trends produced by fractional crystallization.

Decoupling major and trace elements

Namur *et al.* (2014) have shown that most plagioclase crystals from LZa to UZa (and equivalent subzones in the MBS and UBS) have rims buffered to constant compositions of $An_{56\pm2}$ (LZa; Supplementary Data Fig. 1), $An_{50\pm1}$ (LZb) and to a lesser extent $An_{40\pm2}$ (LZc–UZa). They interpreted these patterns as resulting from solidification of the mush liquid during episodes of slow cooling due to enhanced latent heat release at the saturation of a new intercumulus phase. This leads to a progressive decrease of the amount of undercooling, acting in an opposite way to crystal fractionation and maintaining the plagioclase major element composition

relatively constant. Some profiles with buffered rims can be observed in Figure 8. An important observation from this figure is that trace elements do not show the same behaviour and generally evolve continuously from the core to the rim of the plagioclase grains with no zones of constant composition. Although some elements (e.g. Sr) do not show strong compositional variation from core to rim, other elements such as Ba and LREE increase, whereas Ti generally decreases. We believe that the absence of trace element buffering is related to the minor effect of temperature on trace element partitioning between crystals and melt compared to its effect on the equilibrium major element composition (Blundy & Wood, 1994; Namur *et al.*, 2012b, 2014). Assuming a closed system, the evolution of trace elements in the near-isothermal mush liquid is, therefore, dominantly controlled by crystallization of the pore melt (Ross & Elthon, 1997). Decrease of the pore melt volume leads to enrichment in incompatible trace elements and depletion of compatible trace elements. This translates to enrichment or depletion of these elements in equilibrium plagioclase rims which, in contrast to major elements, are, therefore, not buffered to constant trace element concentrations during near-isothermal growth of the rims.

Evolution of compatible and imcompatible trace elements

Effective fractional crystallization of the crystal mush liquid is an efficient way to produce core to rim chemical zoning of cumulus phases. In the following, we use the evolution of compatible and incompatible trace elements from core to rim of plagioclase and clinopyroxene crystals to decipher whether or not fractional crystallization can explain these zoning patterns. We first note that, if upon crystallization the liquid in the crystal mush follows a differentiation trend similar to that of the main magma body (Humphreys, 2009), a complex evolution of trace elements may be expected towards crystal rims (increase, decrease or bell-shaped profiles) depending on their degree of compatibility and the stratigraphic position of the samples:

1. For compatible elements, a continuous decrease in the rim should be observed. Compatible elements in Skaergaard minerals such as Ni and Cr are usually below detection limit in plagioclase. Continuous decrease of Cr is however observed from core to rim in all clinopyroxene crystals that we have measured, consistent with continuous fractional crystallization of the mush liquid (Fig. 11).
2. For elements which are at first incompatible and then become compatible after the saturation of a new, interstitial, phase, a bell-shaped evolution should be observed in the rim. Ti illustrates this behaviour well (Humphreys, 2009, 2011). In rocks from LZa and to a lesser extent LZb, Ti is incompatible before the saturation of intercumulus Fe–Ti oxide minerals and then becomes compatible after the saturation of these minerals (Figs 8 and 9). As a consequence, many rim analyses in plagioclase have higher Ti content than the cores, whereas other rim analyses, corresponding to the crystallization products at lower residual liquid fractions, have lower Ti concentrations than the cores (Fig. 10). From LZc to the top of the LS, Fe–Ti oxide minerals are already saturated and most rim compositions, therefore, have lower Ti contents than the cores of the crystals. Phosphorus is also incompatible before the saturation of interstitial apatite in the crystal mush and in samples containing a significant amount of interstitial material, a bell-shaped profile of P can be observed in plagioclase rims (SIMS analyses; Fig. 9). This also supports the interpretation of fractional crystallization and illustrates that compositional profiles can be used to track the appearance of intercumulus phases in gabbroic crystal mushes (Bernstein, 2006).
3. Incompatible elements should increase continuously from core to rim although the degree of enrichment may be strongly dependent on the minerals crystallizing from the interstitial melt. This behaviour is illustrated by Ba, Sr and Eu for which rim analyses show minor to moderate enrichment compared to the core compositions (Figs 8–10). A more spectacular degree of enrichment is shown by LREE (e.g. Ce) for which rims reach Ce concentrations up to 25 ppm. This is much higher than the highest Ce concentrations in plagioclase cores from the most evolved cumulates of the intrusion (UZc; $F < 0{\cdot}01$; Ce = 4 ppm). We note that Jang & Naslund (2001) report a Ce concentration of 20 ppm in plagioclase from the SH. However, the high Zr content of their analysis ($\sim$ 200 ppm) suggests that their plagioclase separate was contaminated with Zr- and presumably REE-rich accessory minerals. Ce is incompatible in most Skaergaard minerals, with the exception of apatite. It can, therefore, be considered as a highly incompatible element during most of the crystallization of the mush liquid. The extreme enrichment in Ce that we see in plagioclase rims, therefore, suggests that either plagioclase rims record fractionation down to extremely low fraction of residual melt or that some processes contributed to increase the Ce content of the mush liquid to an extent that is not observed in the main magma body. We already note that extreme fractional crystallization seems inconsistent with other elements (e.g. Sr, Ba, Eu) which only show moderate core to rim enrichment (Figs 8 and 9).

Evolution of LREE in plagioclase rims

Modelling fractional crystallization of the mush liquid

In this section, we attempt to model the evolution of the liquid in the crystal mush during fractional crystallization. Using appropriate partition coefficients, we also calculate the evolution of mineral compositions that

form during the crystallization process. We consider that mush liquid solidification dominantly produces rims on existing primocrysts and we compare the results of our models to actual compositions measured in plagioclase crystals. This is then used to discuss whether or not fractional crystallization can explain the compositional profiles observed in the Skaergaard minerals. We particularly focus on Ce, a highly incompatible trace element, which shows extreme degrees of enrichment in the rims of many plagioclase crystals, especially in the LZ (Figs 8–10).

Because of the difficulty inherent in the modelling of crystallization of the mush liquid (see details on the methodology below and in the Supplementary Data), we restricted our effort to a single sample. We simulated fractional crystallization of the mush liquid in a cumulate from LZa (118678) in which we see the strongest zoning patterns (strong and continuous enrichment in Ba and Eu from core to rim, moderate Sr enrichment and extreme Ce enrichment up to 15 ppm; Fig. 8a) and for which we know from textural observations and geochemistry that abundant interstitial liquid crystallized ($\sim$ 40%; Namur *et al.* 2014). Our model attempt to fit the Ce data for the crystal is illustrated in Figure 8. This sample is made up of cumulus plagioclase and olivine as well as interstitial clinopyroxene, Fe–Ti oxides and minor apatite.

An important input parameter for the model is the composition of the interstitial liquid that is initially trapped in the mush at the stratigraphic position of interest in the cumulate column of the Skaergaard intrusion. We consider that it is identical to the liquid in the main magma body that formed the crystal cores (primocrysts) in the sample. The liquid composition can, therefore, be calculated as long as the stratigraphic position of the sample is accurately known. This stratigraphic position can be converted to a fraction of residual liquid (F) in the main magma body using equation 1 in Tegner *et al.* (2009). When F is known, the mush liquid composition is obtained from the models of fractional crystallization of the main magma body presented above.

For sample 118678, its stratigraphic position at -76 m translates to a residual melt fraction in the main Skaergaard magma body (F) of 0·78 (Namur *et al.*, 2014). From this value, we calculated the trace element content of the liquid and assumed that this melt forms the initial mush liquid in chemical equilibrium with the crystal cores forming the matrix of the crystal mush. Such a liquid contains $\sim$ 35 ppm Ce. In order to compare fractional crystallization results with measured plagioclase compositions, we modelled the crystallization history of the crystal from sample 118678 illustrated in Figure 8. According to the detailed profile of the An content (Fig. 8a), we made the initial assumption of a box-shaped crystal with a core size of 900x400x400 μm^3 and a final rim of 300 μm on the (010) crystal face, although we allowed the rim width to vary from 200 to 600 μm We also considered that the extent of rim growth is linearly related to the decrease of the mush liquid fraction during solidification. To model fractional crystallization, we used identical cotectic proportions to those described above for the fractional crystallization of the main magma body. We considered that the interstitial mineral assemblage evolves during solidification of the mush liquid and we used identical residual liquid fractions (Humphreys, 2009) at the appearance of new intercumulus phases (clinopyroxene, Fe–Ti oxides and apatite; Nielsen, 2004) to those used for modelling the crystallization of the main magma body (see above and Supplementary Data). We used average values of partition coefficients described in the Monte Carlo models presented above. We kept the partition coefficients constant for two reasons: (1) average D values commonly offer the best fits to core compositions during fractional crystallization (Figs 15 and 16); (2) using constant D values is appropriate because most plagioclase rims are buffered to a constant major element composition (An content; see Fig. 8 and Namur *et al.*, 2014). In addition, over the entire temperature interval of crystallization of Skaergaard magmas ($\sim$1170–1000°C; Thy *et al.*, 2009b), $D_{Ce}^{Plag/Sil}$ does not change significantly ($\sim$ 0·04–0·06 according to the recent model of Sun *et al.*, 2017).

In Figure 17a, we show the calculated evolution of Ce in a plagioclase crystal from sample 118678 for different rim widths (dotted and dashed lines) and compare the results with LA-ICP-MS and SIMS analyses in the same crystal (squares and circles). The first important observation from Figure 17a and our modelling results is that the degree of REE enrichment in the plagioclase rim (15 ppm) can only be produced by considering that the outermost part of the rim crystallized from an evolved liquid produced at extremely low residual liquid fraction ($<$ 0·01). Given the spot size that we used for *in situ* analyses (30 μm), it is unlikely that we were able to sample the crystal layers formed during the crystallization of the very last droplets of liquid. Furthermore, extreme fractional crystallization seems inconsistent with other elements (e.g. Ba, Sr) which show significantly less enrichment than would be expected at such low residual liquid fractions. We nevertheless note that the behaviour of these elements could have been affected by the crystallization of late-stage phases such as K-feldspar and biotite (Villemant, 1988; Ewart & Griffin, 1994). The second important observation is that simple fractional crystallization only starts to produce strong Ce enrichment at low residual melt fractions (last few μm of the rim), whereas in all crystals that we measured, we observe a continuous Ce increase from the inner to the outer part of the rim (Fig. 17a). Whatever the rim size that we considered in our models (200–600 μm), fractional crystallization cannot produce such a progressive increase. An unrealistically large rim (much larger than suggested by the An profiles) and, therefore, an unrealistically high mush porosity would be required to obtain models fitting the trends of our *in situ* analyses.

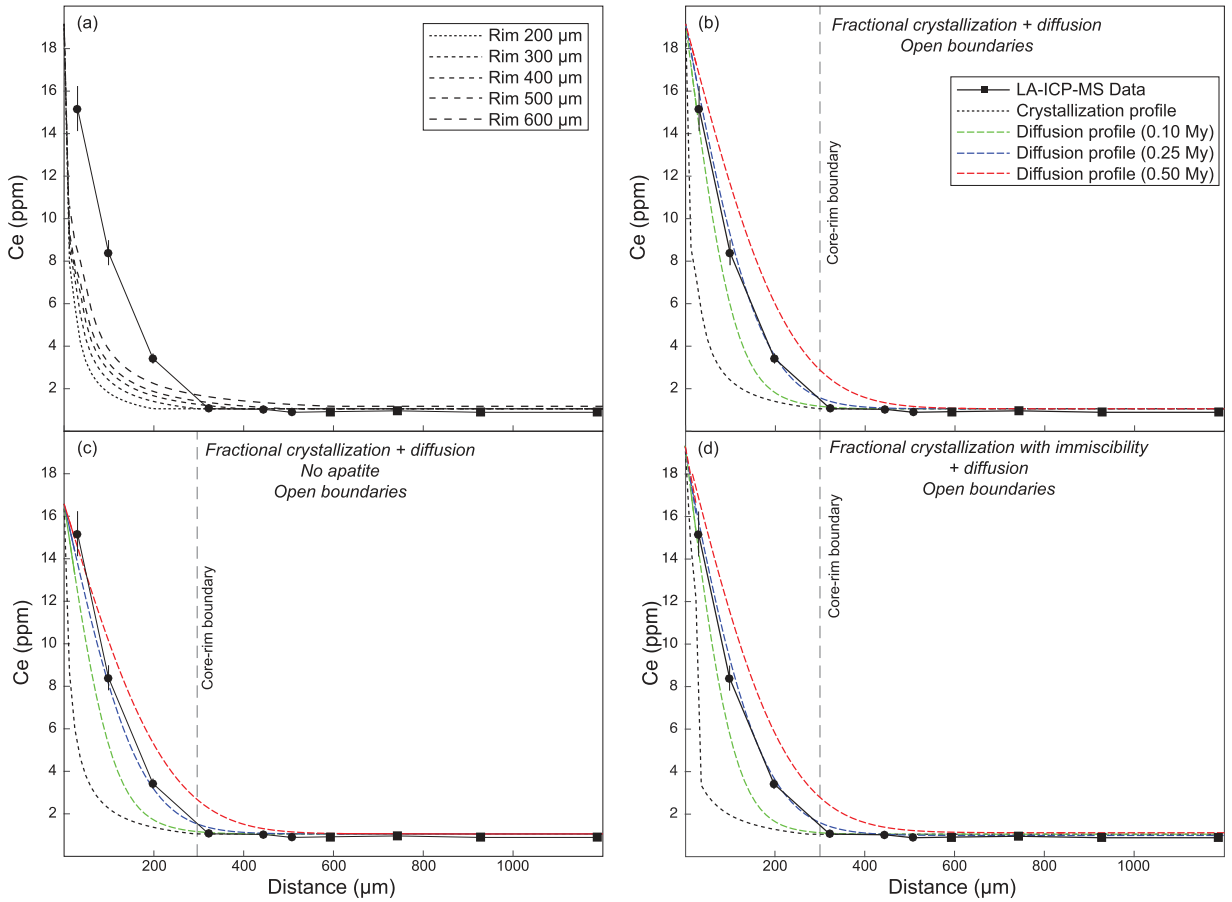

Fig. 17. Plagioclase compositions obtained from theoretical models of fractional crystallization in the crystal mush of LZa, with or without solid-state diffusion, and comparison with chemical data obtained for a plagioclase crystal from sample 118678 (LZa). Fractional crystallization models are calculated using the Rayleigh equation (see details in Supplementary Data) and diffusion models use the methodology described in Costa *et al.* (2008). All models assume that crystal growth is proportional to the decreasing fraction of liquid in the crystal mush. (a) Calculated plagioclase composition obtained by simple fractional crystallization of the mush liquid. Plagioclase trace element composition is calculated from the equilibrium liquid composition using average values of partition coefficients given in the Supplementary Data. We used cotectic proportions from Thy *et al.* (2006) and parental liquid compositions from Nielsen (2004). The model was stopped at F = 0·01. The size of the rim (corresponding to the volume of the plagioclase crystal having crystallized from the mush liquid) was allowed to vary from 200 to 600 μm. For all models, we cannot reproduce the chemical data obtained in sample 118678. (b) Identical model of fractional crystallization with solid-state diffusion of Ce. We considered that the plagioclase rim has a thickness of 300 μm. Diffusion starts when the crystal is fully formed and we calculated diffusion coefficients at 1000°C. (c) Fractional crystallization with solid-state diffusion of Ce in a system that does not crystallize apatite. The model was stopped at F = 0·05 and allows investigation of the effect of apatite on the evolution of Ce during the crystallization of the mush liquid. (d) Fractional crystallization with solid-state diffusion of Ce and development of silicate–liquid immiscibility. We considered that the plagioclase rim crystallized from an Fe-rich immiscible melt and its composition was calculated using average partition coefficients values from Schmidt *et al.* (2006) and Veksler *et al.* (2006). Additional details are given in the text. The model was stopped at F = 0·05.

Compositional boundary layers around plagioclase crystals

Strong enrichment in Ce together with more modest enrichment in other elements (e.g. Ba, Sr, Eu) in plagioclase rims could possibly result from crystallization in a compositional boundary layer developing around crystals (Bernstein, 2006). Such layers develop and stay stable when the growth rate of the crystals significantly exceeds the diffusivity of the chemical components in the melt (Albarede & Bottinga, 1972; Blundy, 1997, Holycross & Watson, 2016). In Skaergaard, the development of boundary layers around crystals is difficult to evaluate because no direct estimates of crystal growth rates have been proposed. However, we think that the development of such layers in the Skaergaard crystal mush is unlikely for at least three reasons: (1) LREE diffusivity in a basaltic melt is 1–2 orders of magnitude higher than the diffusivity of Ti (Zhang *et al.*, 2010). If boundary layers enriched in incompatible elements were forming we would, therefore, also expect a strong enrichment of Ti in plagioclase rims (Meurer & Claeson, 2002), which is generally not observed (Humphreys, 2009); (2) during the early stages of crystal mush solidification, the porosity of the mush is sufficiently high to allow liquid advection (Namur *et al.*, 2014). This allows new, fresh melt from the crystal mush and away from

any crystal to be brought continuously to the crystallization sites and would prevent any boundary layer from developing. In the plagioclase profiles that we measured, we see that Ce concentrations already increase in the innermost part of the plagioclase rims. This could only happen if boundary layers were forming at high residual porosity, which is highly unlikely; and (3) the fluid flow models from Kerr (1995) together with estimated cation diffusivities in basaltic melts (Zhang *et al.*, 2010) suggest that if a boundary layer develops around cumulus crystals, its thickness for LREE must be thinner than 50 μm We do not observe oscillatory zoning for LREE which further supports the absence of compositional boundary layers around plagioclase crystals during the solidification of the mush liquid. Finally, we note that disequilibrium uptake of REE in crystals becomes only important when the crystal growth rate exceeds 10^{-8} m/s (Holycross & Watson, 2016). This value is much higher than the expected crystal growth rates of plagioclase in shallow magmatic systems (10^{-11} to 10^{-12} m/s; Cashman, 1993).

Diffusion of Ce from a liquid film or clinopyroxene

Strong and progressive enrichment of incompatible trace elements in plagioclase rims could originate from solid-state diffusion of these trace elements into the plagioclase lattice. It is known that, at low residual liquid fractions, a melt may form a thin film around crystals (Holness *et al.*, 2007a; Humphreys, 2009) and may become highly enriched in incompatible trace elements (Hiraga *et al.*, 2004). Such a film may stay liquid until the temperature reaches ~ 700°C (Larsen *et al.*, 1992), possibly due to the difficulties of nucleation in small spaces (Holness *et al.*, 2007a), and may be considered as a source of trace elements for the crystals during a diffusion process (Morse & Nolan, 1984). We modelled the diffusion process (see Supplementary Data) in plagioclase in order to estimate if solid state diffusion can explain the compositional profiles observed in sample 118678 (Fig. 17b). Modelling was performed using the standard formalism of Fick's second law (Costa *et al.*, 2008). We used our calculated fractional crystallization profile (rim of 300 μm; Fig. 17a) as the initial compositional profile. We assumed that plagioclase growth stops when the temperature reaches ~ 1000°C (Humphreys, 2009; Thy *et al.*, 2009b) and we used a diffusion coefficient reported for transport normal to (010) in a plagioclase with a composition of An_{67} (Cherniak, 2003). Our models show that with diffusion over 0·1–0·25 Myr, we can reproduce very well the shape of the measured Ce profile with progressive enrichment from the inner part to the outer part of the rim (Fig. 16b). This is a minimum estimate because the temperature of the cumulate is likely to decrease with time so that diffusion gets progressively slower. There is geological evidence to support a role for diffusion in controlling zoning profiles in Skaergaard minerals. The timescales that we calculate are in excellent agreement with cooling rates estimated for the Skaergaard using cation ordering in pyroxenes (0·1–0·3 Myr between 1000 and 700°C, below which diffusion is too slow to modify REE distributions; Ganguly & Domeneghetti, 1996). These timescales are also in agreement with those estimated for solid-state diffusion in the oceanic crust (VanTongeren *et al.*, 2008; Coogan & O'Hara, 2015). Explaining the very high Ce concentrations at the edge of the plagioclase crystals still requires an initial zoning profile (or interstitial melt) that reaches very high Ce contents. As stated above, such a profile can be achieved by extreme fractional crystallization. However, this implies that all plagioclase crystals with strong enrichment in Ce were in contact with a highly evolved residual melt formed at $F < 0{\cdot}01$. This seems extremely unlikely, but not impossible because the last drops of residual melts usually form granophyric pockets commonly located between plagioclase crystals (Holness, 2015). Extreme fractionation should also lead to enrichments in Sr and Ba much stronger than those observed in plagioclase rims. However, initial strong zoning patterns for those elements can easily smoothed during the diffusion process. This could explain the progressive decrease of Ba concentrations that extends from the rim to the central part of the core (Fig. 8). Such a profile can indeed be adequately modelled by extreme fractional crystallization (down to $F = 0{\cdot}01$), followed by solid-state diffusion with a re-equilibration timescale of 0·1–0·25 Myr (Supplementary Data Fig. 7).

Recently it has been suggested that the decoupling between incompatible elements (e.g. Ce) in clinopyroxene and plagioclase from oceanic gabbros could be due to solid-state re-equilibration between these two minerals (Coogan & O'Hara, 2015). This would result from changing $D_{Ce}^{Plag/Cpx}$ with temperature during subsolidus cooling. Using the equations of Wood & Blundy (1997) and Dohmen & Blundy (2014), we calculated that $D_{Ce}^{Plag/Cpx}$ may change, for example, from 0·36 at 1000°C to 0·49 at 800°C. These results are in perfect agreement with the new models of Sun & Liang (2017). This indicates that not only late-stage liquid films but also clinopyroxene could represent a source of Ce for diffusion in plagioclase. In a single sample for which we measured a compositional profile through adjacent clinopyroxene and plagioclase crystals, we observed a decrease of the Ce in the clinopyroxene rim and an increase in the plagioclase rim (Fig. 13), which supports solid-state re-equilibration between these two minerals (Coogan & O'Hara, 2015). However, most clinopyroxene rims are also extremely enriched in Ce (Fig. 12), which indicates that a process other than diffusion must contribute to the enrichment in highly incompatible elements for several minerals formed in the crystal mush of the Skaergaard intrusion.

Delaying apatite crystallization in the mush liquid

An easier way to explain the enrichment in Ce in plagioclase and clinopyroxene rims would be to produce interstitial melts strongly enriched in highly incompatible trace elements at relatively high residual melt fraction,

i.e. high mush porosity. In a study of trace element zoning in cumulus phases in gabbroic rocks from the Apennine ophiolites, Tribuzio *et al.* (1999) have shown that the behaviour of REE in clinopyroxene rims is strongly influenced by the presence or absence of apatite in the rock. This is because $D_{REE}^{Ap/Sil}$ (2–50; Watson & Green 1981) is much higher than D between any other cumulus phase and the silicate melt (< 0·25; Cawthorn 2013). In the main Skaergaard magma body, apatite saturates at the bottom of UZb, when the residual liquid fraction is ~ 0·1 (Nielsen, 2004). At this degree of evolution, the cores of plagioclase crystals show little enrichment in LREE (e.g. Ce 1–2 ppm). If apatite saturation is delayed in the mush liquid because of the thermal regime of the mush (Brandeis & Jaupart, 1987) or the absence of supersaturation in apatite components (Morse, 2011), much higher concentrations of LREE can be expected in the interstitial liquid and, therefore, in the rims of plagioclase crystals. Apatite saturation depends on both liquid composition and temperature (Harrison & Watson, 1984; Tollari *et al.*, 2006). Namur *et al.* (2014) have shown that a significant part of the mush liquid crystallization in Skaergaard occurs in a system which is thermally buffered. As a consequence, it is possible that apatite saturation is reached at lower residual liquid fraction in the crystal mush than in the main magma body. Apatite saturation would only occur in the crystal mush when the mush liquid has cooled down below the temperature of apatite saturation in the main magma body (ca. 1060°C; Thy *et al.*, 2009b).

A potential way to estimate the timing of apatite saturation in the interstitial liquid and to compare with apatite saturation in the main Skaergaard magma body would be to compare the relationship between phosphorous content and An content in plagioclase rims which crystallized from the mush liquid, and in plagioclase cores from the whole stratigraphic column, crystallized from the main magma body (Fig. 5). By doing so, we could estimate if P in plagioclase along a traverse from core to rim starts dropping due to the crystallization of interstitial apatite when a composition of An_{40} (i.e. An content of plagioclase cores at the bottom of UZb) is reached in the rim. In contrast, if P starts dropping at a position in the plagioclase rims where the An content is lower than An_{40}, this would mean that apatite saturation is delayed in the mush liquid. This, however, cannot be achieved for two practical reasons: (1) zoned crystals are only abundant in LZ and in UZ. Above UZb, the main magma body is saturated in apatite as is the crystal mush liquid so that P would continuously decrease in plagioclase rims. In LZ and UZa, where the main magma body is not saturated in apatite, plagioclase rims are usually buffered to a constant An content (Namur *et al.*, 2014). Therefore, they never reach An contents as low as An_{40} (Fig. 3). Some SIMS profiles however show a bell-shaped phosphorous profile from crystal core to crystal rim (Fig. 9b), indicating that apatite ultimately saturates in the interstitial liquid from the crystal mush; and (2) the vast majority of our rim analyses were performed by LA-ICP-MS and the signal-to-noise ratio for P was found to be too low to be used (see above).

Another way to test the timing of apatite saturation in the crystal mush is to compare the trace element contents of interstitial apatite (LZa–UZa) and cumulus apatite (UZb–UZc). REE concentrations in interstitial and cumulus apatites support delayed saturation of apatite in the crystal mush during the formation of the LZ, MZ and UZa. Our new analyses (Supplementary Dataset 10) together with published data (Nash, 1976; Jang, 2001) show that the LREE (e.g. Ce) content of interstitial apatite that crystallized from the liquid in the crystal mush is the highest in LZa–LZb, and decreases upwards to reach minimum values at the bottom of UZb. In cumulus apatite that crystallized from the main magma body, Ce concentrations then strongly increase in UZb–UZc. Higher concentrations of LREE in interstitial apatite from LZa–LZb compared to the first cumulus apatite from UZb suggests that apatite saturation was indeed reached at a higher degree of liquid fractionation (i.e. lower melt fraction) in the mush liquid of the LZ than in the main magma body.

We have modelled the evolution of Ce in plagioclase rims by making the assumption that apatite does not crystallize (or only very late) in the mush liquid (Fig. 17c) to estimate if this process could explain the concentrations of LREE observed in plagioclase rims. The degree of Ce enrichment in the outer part of the rim can be reproduced when the residual mush liquid fraction is 0·05. As this value is relatively close to the permeability threshold in cumulate rocks (Cheadle *et al.*, 2004), it is realistic to consider that most plagioclase crystals were in contact with this evolved melt. However, simply delaying apatite crystallization is not sufficient to produce the Ce profiles that we see in plagioclase rims, and especially the continuous Ce increase throughout the rims (from the inner part to the outer part of the rims). Solid-state diffusion for 0·1–0·25 Myr is still needed to match the measured profiles (Fig. 17c). Also, delaying apatite cannot be considered as a realistic process in the crystal mush forming in UZb and UZc where some plagioclase rims show extreme Ce enrichment (Fig. 10).

Development of silicate liquid immiscibility in the crystal mush

Silicate liquid immiscibility developed in the main magma body (Jakobsen *et al.*, 2005) and the crystal mush (Holness *et al.*, 2011; Humphreys, 2011) of the Skaergaard intrusion. In the main magma body, both immiscible melts stay in equilibrium and immiscibility has no effect on mineral compositions (Charlier *et al.*, 2011). In contrast, immiscibility in the crystal mush is known to produce mineral compositions and mineral assemblages that are not observed in the cumulus phases (Holness

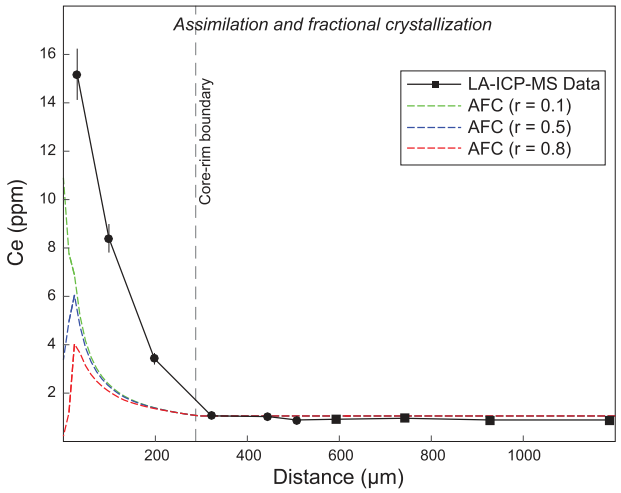

Fig. 18. Plagioclase compositions obtained from theoretical model of assimilation and fractional crystallization (AFC) in the LZa crystal mush and comparison with chemical data obtained for a plagioclase crystal from sample 118678 (LZa). AFC was modelled using the methodology of Lissenberg *et al.* (2013), the equations of DePaolo (1981) and cotectic proportions from Thy *et al.* (2006). Calculations used average values of partition coefficients given in the Supplementary Data. r, ratio of assimilated/fractionated material.

et al., 2011). This is because immiscible melts may be physically separated in the crystal mush (Holness *et al.*, 2011; Nielsen *et al.*, 2015), and, therefore, evolve along their own liquid lines of descent and produce different mineral compositions (Humphreys, 2011). Using the Skaergaard liquid line of descent proposed by Nielsen *et al.*, (2009) and a parameterization for the onset of silicate liquid immiscibility based on experiments from Charlier & Grove (2012), we estimated that immiscibility is likely to develop at F = 0·2 (UZa) and that the relative proportions of Fe-rich melt and Si-rich melt may initially be ~ 0·25 and ~ 0·75, respectively. This is in good agreement with previous estimates (Jakobsen *et al.*, 2011; Nielsen *et al.*, 2015). Using our models of fractional crystallization of the main magma body, we calculated that the Ce content of the last homogeneous melt before immiscibility would contain ~ 90 ppm of Ce. Using this value and partition coefficients between immiscible melts ($D_{LREE}^{Fe-melt/Si-melt}$: 2–5; Schmidt *et al.*, 2006; Veksler & Charlier 2015), we calculated that, at the onset of immiscibility, the Fe-rich melt would contain 142 ± 18 ppm of Ce while the Si-rich melt would contain 72 ± 6 ppm of Ce. Immiscible melts have contrasting densities (Fe-rich melt: 2·9–3·1 g/cm^3; Si-rich melt: 2·4–2·5 g/cm^3; Namur *et al.*, 2015), which may lead to the segregation of the Si-rich melt from the crystal mush (Holness *et al.*, 2011; Nielsen *et al.*, 2015). It is, therefore, reasonable to suggest that part of the plagioclase rims may have crystallized from a dominantly Fe-rich immiscible melt which has the potential to create rims strongly enriched in incompatible trace elements (e.g. Ce) and only moderately enriched in mildly compatible trace elements. We modelled the crystallization of plagioclase rims from a Fe-rich melt (Fig. 17d). This process may easily produce rims strongly enriched in Ce at relatively high F (0·05), but again is not capable of producing a continuous Ce increase from the inner part to the outer part of the rim. Furthermore, such rims would also be expected to be An-rich, due to Ca partitioning in the Fe-rich melt that lost physical equilibrium with the conjugate Si-rich melt (Holness *et al.*, 2011; Humphreys, 2011), whereas we see high Ce (~ 18 ppm) in plagioclase rims of An_{30} adjacent to pockets of granophyre (Fig. 9).

Immiscibility may play a role in decoupling the behaviour of REE and Zr in clinopyroxene, particularly in the UZ. As shown in Figure 12, Ce and Y concentrations in rims from the UZ are higher than those of the LZ at any given Zr content. As discussed above, this cannot be explained by a change of substitution mechanism due to changing major element composition. Experimental data show that Ce and Y partition more strongly into the immiscible Fe-rich melt than Zr (Schmidt *et al.*, 2006; Veksler *et al.*, 2006). Early immiscibility in the UZ mush as opposed to late-stage immiscibility in the LZ mush could, therefore, be an efficient way of producing strong enrichment in REE and decoupling REE from Zr in clinopyroxenes rims from the UZ that may have crystallized from a dominantly Fe-rich immiscible melt.

Other processes possibly affecting the distribution of trace elements

It has been suggested that infiltration of metasomatic melts may be an important process to enrich plagioclase and clinopyroxene rims in highly incompatible elements (O'Reilly & Griffin, 1988; Roex & Class, 2016). Although the closed nature of the Skaergaard intrusion argues against the infiltration of external melts, migration of interstitial melt in the crystal mush may, however, occur by compositional convection (Toplis *et al.*, 2008) and/or crystal mush compaction (Tegner *et al.*, 2009). Compositional convection essentially brings to the mush a liquid which has a composition identical to that of the main magma body and removes evolved interstitial melts from the crystallization sites. As a consequence, compositional convection should lead to the formation of crystals with little reverse zoning or no zoning at all (Toplis *et al.*, 2008). This process is, therefore, not capable of producing plagioclase and clinopyroxene rims with extremely high concentrations of incompatible trace elements.

Compaction of the crystal mush expels evolved interstitial melt from the crystal matrix towards the main magma body. In the simplest case, migration of interstitial melt can produce cumulus crystals with normal zoning (Humphreys, 2009). However, simple migration of interstitial melt cannot produce plagioclase rims significantly more enriched in incompatible elements than the most evolved plagioclase cores at the top of UZc. Migration of interstitial melt in the crystal mush can also produce dissolution of cumulus phases and re-

crystallization of minerals with another composition (Namur *et al.*, 2013). Such a process requires a strong chemical and, or, thermal disequilibrium between the infiltrating melt and the crystal matrix. In Skaergaard, this process was shown to occur during the infiltration of hot, primitive melt with low concentrations of incompatible trace elements (Namur *et al.*, 2013). Nevertheless, for other gabbroic rocks in the Bushveld complex (Mathez, 1995) and in the oceanic crust (Lissenberg *et al.*, 2013), the process of assimilation-fractional crystallization (AFC) was adequately used to explain strong decoupling between trace elements, as well as geochemical trends significantly departing from simple fractional crystallization (e.g. primitive pyroxene crystals with high REE concentrations; Mathez 1995). We modelled the effect of AFC using the equations of DePaolo (1981). The AFC process is indeed capable of producing decoupling between highly incompatible elements (e.g. Ce) and mildly compatible elements (e.g. Sr, Ba). However, such a decoupling is only observed for high ratios of assimilated material/crystallized material (e.g. $r = Ma/Mc > 0{\cdot}8$). With such a high value of r, strong enrichment in LREE in plagioclase rims is impossible because the REE concentration drops when the mush liquid becomes saturated in apatite (Fig. 18). There are other issues which make the process of AFC highly unlikely: (1) high values of r imply strong dissolution of crystal cores. No obvious dissolution textures were reported in cumulates from the LS in which we observe some of the strongest zoning patterns in plagioclase and clinopyroxene crystals; and (2) compaction was shown to be inefficient in most of the lower part of the Skaergaard LS (Tegner *et al.*, 2009) where there is no obvious driving force for intense melt migration in the crystal mush.

Exsolution of a free hydrous fluid phase from basaltic magmas is considered as an important mechanism for large-scale leaching, transport and precipitation of metals (Boudreau & McCallum, 1989; Boudreau, 2008). Hydrous, chlorine-rich fluids may also carry abundant Cl-complexed trace elements such as the REE (possibly excepting Eu^{2+}; Haas *et al.*, 1995; Boudreau & McCallum 1989). In Skaergaard, the presence of a Cl-rich, free fluid phase during solidification of the crystal mush was recognized by trapped fluid inclusions in crystals (Larsen *et al.*, 1992). The presence of such a fluid in the pore spaces between primocrysts could contribute to the enrichment in REE that we observe in plagioclase and clinopyroxene rims (Mathez, 1995; McBirney & Sonnenthal, 1990). However, we think that this process is of minor importance for several reasons: (1) the development of a fluid phase in Skaergaard occurred when the crystal mush was very close to the solidus temperature (i.e. 770–650°C; Larsen *et al.*, 1992). The fluid phase coexisted with a volumetrically minor melt phase that only formed some granophyric pockets and gabbroic pegmatites (Larsen *et al.*, 1992). Therefore such a fluid phase cannot have coexisted with the melt that formed plagioclase and clinopyroxene rims locally exceeding 500 μm in width. At this temperature, diffusion is also too slow to reequilibrate plagioclase rims that were already formed. In addition, the mobility of the fluid phase in the crystal mush was negligible and large-scale mobility only occurred where the permeability of the mush was increased by local faulting or block foundering (McBirney & Sonnenthal, 1990). There is no petrographic or geochemical evidence for a pervasive and intrusion-wide fluid phase at Skaergaard and where fluid was mobile and reacted with primocrysts, cumulate rocks are replaced by pegmatitic bodies and, or, anorthosite (McBirney & Sonnenthal, 1990). All the samples that we investigated are fresh troctolites and gabbros suggesting that they were not affected by a metasomatic agent; and (2) although the Skaergaard fluid phase is thought to be highly enriched in Cl ($\sim$ 20 wt % NaCl; Larsen *et al.*, 1992), partition coefficients for the LREE between the fluid phase and the silicate melt ($D_{LREE}^{Fluid/Melt}$) are significantly lower than 1 ($\sim$ 0·01–0·5; Flynn & Burnham, 1978; Adam *et al.*, 1997, 2014; Zajacz *et al.*, 2008). As a consequence, the fluid phase carries less LREE than the equilibrium silicate melt and cannot contribute to LREE enrichment in crystals to an extent that cannot be achieved by simple crystallization of the interstitial silicate melt.

CONCLUSIONS

Major elements in plagioclase and clinopyroxene vary continuously from the bottom to the top of the Skaergaard intrusion, suggesting that the magma chamber differentiated through efficient fractional crystallization. Our new data on trace elements (LA-ICP-MS) in these two minerals show that core compositions also change continuously from base to top, with compatible elements being progressively depleted whereas incompatible elements become progressively enriched. Numerical models indicate that the behaviour of trace elements can be broadly explained within the context of fractional crystallization. Nevertheless, the evolution of some elements, especially the LREE, can only be partly reproduced by fractional crystallization models. Ba concentrations in plagioclase and clinopyroxene also show values lower than expected from simple fractional crystallization, especially in the upper part of the intrusion where the residual liquid fraction is less than 20 %. At this stage of magma chamber solidification, fractional crystallization probably becomes less effective in an almost fully solid magma chamber and is replaced by a major proportion of *in situ*, equilibrium crystallization.

Our detailed *in situ* (LA-ICP-MS and SIMS) analyses of plagioclase and clinopyroxene overgrowths also allowed us to investigate the behaviour of trace elements during the solidification of the interstitial melt in a crystal mush. An important observation is that trace elements in mineral rims allow us to track the evolution of the melt during crystallization. In particular, the bell-shaped profiles of Ti and P from core to rim indicate saturation of Fe–Ti oxides and apatite in the crystal mush.

Continuous increase of highly- to moderately-incompatible elements mimics the stratigraphic trends observed in plagioclase and clinopyroxene cores, indicating that the mush liquid also differentiated through fractional crystallization. However, some elements, and in particular the LREE, show trends departing significantly from those observed in crystal cores. LREE concentrations in plagioclase rims are always much higher than the most evolved crystal cores in the SH. Although such high REE concentrations could possibly be produced by fractional crystallization at low residual liquid fraction, such a process cannot explain the strong and continuous enrichment in LREE from the inner part to the outer part of the rims. We argue that the distribution of LREE in rims of Skaergaard minerals is affected by the timing of apatite saturation and the development of silicate liquid immiscibility in the crystal mush. It is then modified by solid-state diffusion either between adjacent mineral grains (e.g. plagioclase and clinopyroxene) or between minerals and thin films of late-stage liquid. In contrast, we believe that neither the exsolution of a free fluid phase, nor interstitial liquid migration by compaction or compositional convection played a significant role in controlling the distribution of trace elements in Skaergaard minerals.

ACKNOWLEDGMENTS

O. N. was supported by a Junior Research Fellowship at Magdalene College, University of Cambridge and an Intra-European Individual Marie Curie Fellowship at the University of Hannover. M.C.S.H. was supported by a Royal Society University Research Fellowship. This work was supported by the Natural Environment Research Council through a grant number (NE/F020325/I) and access to the Edinburgh Ion Microprobe Facility (IMF-433–0511). J. Day (Cambridge) and I. Horn (Hannover) are thanked for their help with LA-ICP-MS analyses. C. J. de Hoog and the Ion Microprobe Facility Staff at the University of Edinburgh are thanked for their help with SIMS analyses. Kathi Faak is thanked for her help with diffusion modelling. I. Buisman is thanked for her help with EPMA analyses. Troels Nielsen is thanked for providing samples from the Bollinberg profile. Discussions with M Holness, C. Tegner, F. Holtz, B. Charlier and T. Nielsen were highly appreciated.

SUPPLEMENTARY DATA

Supplementary data are available at *Journal of Petrology* online.

REFERENCES

Adam, J., Green, T. H., Sie, S. H. & Ryan, C. G. (1997). Trace element partitioning between aqueous fluids, silicate melts and minerals. *European Journal of Mineralogy* **9**, 569–584.

Adam, J., Locmelis, M., Afonso, J. C., Rushmer, T. & Fiorentini, M. L. (2014). The capacity of hydrous fluids to transport and fractionate incompatible elements and metals within the Earth's mantle. *Geochemistry, Geophysics, Geosystems* **15**, 2241–2253.

Aigner-Torres, M., Blundy, J., Ulmer, P. & Pettke, T. (2007). Laser ablation ICPMS study of trace element partitioning between plagioclase and basaltic melts: an experimental approach. *Contributions to Mineralogy and Petrology* **153**, 647–667.

Albarede, F. & Bottinga, Y. (1972). Kinetic disequilibrium in trace element partitioning between phenocrysts and host lava. *Geochimica et Cosmochimica Acta* **36**, 141–156.

Barnes, S. J. (1986). The effect of trapped liquid crystallization on cumulus mineral compositions in layered intrusions. *Contributions to Mineralogy and Petrology* **93**, 524–531.

Beattie, P., Drake, M., Jones, J., Leeman, W., Longhi, J., McKay, G., Nielsen, R., Palme, H., Shaw, D. & Takahashi, E. (1993). Terminology for trace-element partitioning. *Geochimica et Cosmochimica Acta* **57**, 1605–1606.

Bédard, J. (2006). Trace element partitioning in plagioclase feldspar. *Geochimica et Cosmochimica Acta* **70**, 3717–3742.

Bédard, J. (2014). Parameterizations of calcic clinopyroxene—melt trace element partition coefficients. *Geochemistry, Geophysics, Geosystems* **15**, 303–336.

Bédard, J. (2015). Ophiolitic magma chamber processes, a perspective from the Canadian Appalachians. In: Charlier, B., Namur, O., Latypov, R., & Tegner, C. (eds) *Layered Intrusions*. Netherlands: Springer. pp. 693–732.

Bédard, J. H., Marsh, B. D., Hersum, T. G., Naslund, H. R. & Mukasa, S. B. (2007). Large-scale mechanical redistribution of orthopyroxene and plagioclase in the Basement Sill, Ferrar dolerites, Antarctica: petrological, mineral-chemical and field evidence for channelized movement of crystals and melt. *Journal of Petrology* **48**, 2289–2326.

Bernstein, S. (2006). In situ fractional crystallization of a mafic pluton: microanalytical study of a palaeogene gabbronorite plug in east Greenland. *Lithos* **92**, 222–237.

Bindeman, I. N. & Davis, A. M. (2000). Trace element partitioning between plagioclase and melt: investigation of dopant influence on partition behavior. *Geochimica et Cosmochimica Acta* **64**, 2863–2878.

Bindeman, I. N., Davis, A. M. & Drake, M. J. (1998). Ion microprobe study of plagioclase-basalt partition experiments at natural concentration levels of trace elements. *Geochimica et Cosmochimica Acta* **62**, 1175–1193.

Blundy, J. (1997). Experimental study of a Kiglapait marginal rock and implications for trace element partitioning in layered intrusions. *Chemical Geology* **141**, 73–92.

Blundy, J. D. & Wood, B. J. (1991). Crystal-chemical controls on the partitioning of Sr and Ba between plagioclase feldspar, silicate melts, and hydrothermal solutions. *Geochimica et Cosmochimica Acta* **55**, 193–209.

Blundy, J. D. & Wood, B. J. (1994). Prediction of crystal-melt partition coefficients from elastic moduli. *Nature* **372**, 452–454.

Boudreau, A. E. (2008). Modeling the Merensky Reef, Bushveld Complex, Republic of South Africa. *Contributions to Mineralogy and Petrology* **156**, 431–437.

Boudreau, A. E. & McCallum, I. S. (1989). Investigations of the Stillwater Complex: part V. Apatites as indicators of evolving fluid composition. *Contributions to Mineralogy and Petrology* **102**, 138–153.

Brandeis, G. & Jaupart, C. (1987). The kinetics of nucleation and crystal growth and scaling laws for magmatic crystallization. *Contributions to Mineralogy and Petrology* **96**, 24–34.

Carpenter, P., Counce, D., Kluk, E. & Nabelek, C. (2002). Characterization of EPMA standard glasses 95IRV, 95IRW,

and 95IRX. *Journal of Research of the National Institute of Standards and Technology* **107**, 703–718.
Cashman, K. V. (1993). Relationship between plagioclase crystallization and cooling rate in basaltic melts. *Contributions to Mineralogy and Petrology* **113**, 126–142.
Cawthorn, R. G. (2013). Rare earth element abundances in apatite in the Bushveld Complex: a consequence of the trapped liquid shift effect. *Geology* **41**, 603–606.
Cawthorn, R. G. & Tegner, C. (2017). Modeling incompatible trace-element abundances in plagioclase in the Skaergaard intrusion using the trapped liquid shift effect. *Contributions to Mineralogy and Petrology* **172**, 93.
Charlier, B. & Grove, T. L. (2012). Experiments on liquid immiscibility along tholeiitic liquid lines of descent. *Contributions to Mineralogy and Petrology* **164**, 27–44.
Charlier, B., Namur, O., Toplis, M. J., Schiano, P., Cluzel, N., Higgins, M. D. & Vander Auwera, J. (2011). Large-scale silicate liquid immiscibility during differentiation of tholeiitic basalt to granite and the origin of the Daly gap. *Geology* **39**, 907–910.
Cheadle, M. J., Elliott, M. T. & McKenzie, D. (2004). Percolation threshold and permeability of crystallizing igneous rocks: the importance of textural equilibrium. *Geology* **32**, 757–760.
Cherniak, D. (2003). REE diffusion in feldspar. *Chemical Geology* **193**, 25–41.
Cherniak, D. J. & Watson, E. B. (1994). A study of strontium diffusion in plagioclase using Rutherford backscattering spectroscopy. *Geochimica et Cosmochimica Acta* **58**, 5179–5190.
Coogan, L. A. & O'Hara, M. J. (2015). MORB differentiation: in situ crystallization in replenished-tapped magma chambers. *Geochimica et Cosmochimica Acta* **158**, 147–161.
Coogan, L. A., Kempton, P. D., Saunders, A. D. & Norry, M. J. (2000a). Melt aggregation within the crust beneath the mid-atlantic ridge: evidence from plagioclase and clinopyroxene major and trace element compositions. *Earth and Planetary Science Letters* **176**, 245–257.
Coogan, L. A., Saunders, A. D., Kempton, P. D. & Norry, M. J. (2000b). Evidence from oceanic gabbros for porous melt migration within a crystal mush beneath the Mid-Atlantic Ridge. *Geochemistry, Geophysics, Geosystems* **1**, doi: 10.1029/2000GC000072.
Costa, F., Dohmen, R. & Chakraborty, S. (2008). Time scales of magmatic processes from modeling the zoning patterns of crystals. *Reviews in Mineralogy and Geochemistry* **69**, 545–594.
DePaolo, D. J. (1981). Trace element and isotopic effects of combined wallrock assimilation and fractional crystallization. *Earth and Planetary Science Letters* **53**, 189–202.
Dohmen, R. & Blundy, J. (2014). A predictive thermodynamic model for element partitioning between plagioclase and melt as a function of pressure, temperature and composition. *American Journal of Science* **314**, 1319–1372.
Dygert, N., Liang, Y., Sun, C. & Hess, P. (2014). An experimental study of trace element partitioning between augite and Fe-rich basalts. *Geochimica et Cosmochimica Acta* **132**, 170–186.
Ewart, A. & Griffin, W. (1994). Trace-element partitioning with application to magmatic processes application of proton-microprobe data to trace-element partitioning in volcanic rocks. *Chemical Geology* **117**, 251–284.
Flynn, R. T. & Burnham, C. W. (1978). An experimental determination of rare earth partition coefficients between a chloride containing vapor phase and silicate melts. *Geochimica et Cosmochimica Acta* **42**, 685–701.
Fujimaki, H. (1986). Partition coefficients of Hf, Zr, and REE between zircon, apatite, and liquid. *Contributions to Mineralogy and Petrology* **94**, 42–45.
Gaetani, G. A. & Grove, T. L. (1997). Partitioning of moderately siderophile elemenrts among olivine, silicate melt, and sulfide melt: constraints on core formation in the Earth and Mars. *Geochimica et Cosmochimica Acta* **61**, 1829–1846.
Ganguly, J. & Domeneghetti, C. M. (1996). Cation ordering of orthopyroxenes from the Skaergaard intrusion: implications for the subsolidus cooling rates and permeabilities. *Contributions to Mineralogy and Petrology* **122**, 359–367.
Giordano, D., Russell, J. K. & Dingwell, D. B. (2008). Viscosity of magmatic liquids: a model. *Earth and Planetary Science Letters* **271**, 123–134.
Haas, J. R., Shock, E. L. & Sassani, D. C. (1995). Rare earth elements in hydrothermal systems: estimates of standard partial molal thermodynamic properties of aqueous complexes of the rare earth elements at high pressures and temperatures. *Geochimica et Cosmochimica Acta* **59**, 4329–4350.
Harrison, T. M. & Watson, E. B. (1984). The behavior of apatite during crustal anatexis: equilibrium and kinetic considerations. *Geochimica et Cosmochimica Acta* **48**, 1467–1477.
Hart, S. R. & Davis, K. E. (1978). Nickel partitioning between olivine and silicate melt. *Earth and Planetary Science Letters* **40**, 203–219.
Hermann, J., Müntener, O. & Günther, D. (2001). Differentiation of mafic magma in a continental crust-to-mantle transition zone. *Journal of Petrology* **42**, 189–206.
Hiraga, T., Anderson, I. M. & Kohlstedt, D. L. (2004). Grain boundaries as reservoirs of incompatible elements in the Earth's mantle. *Nature* **427**, 699–703.
Hirschmann, M. M., Renne, P. R. & McBirney, A. R. (1997). $^{40}Ar^{39}Ar$ dating of the Skaergaard intrusion. *Earth and Planetary Science Letters* **146**, 645–658.
Holness, M. B. (2015). Plagioclase growth rates control three-grain junction geometry in dolerites and gabbros. *Journal of Petrology* **56**, 2117–2144.
Holness, M. B., Anderson, A. T., Martin, V. M., MacLennan, J., Passmore, E. & Schwindinger, K. (2007a). Textures in partially solidified crystalline nodules: a window into the pore structure of slowly cooled mafic intrusions. *Journal of Petrology* **48**, 1243–1264.
Holness, M. B., Cawthorn, R. G. & Roberts, J. (2017b). The thickness of the crystal mush on the floor of the Bushveld magma chamber. *Contributions to Mineralogy and Petrology* **172**, 102.
Holness, M. B., Namur, O. & Cawthorn, R. G. (2013). Disequilibrium dihedral angles in layered intrusions: a microstructural record of fractionation. *Journal of Petrology* **54**, 2067–2093.
Holness, M. B., Nielsen, T. F. D. & Tegner, C. (2017c). The Skaergaard intrusion of East Greenland: paradigms, problems and new perspectives. *Elements* **13**, 391–396.
Holness, M. B., Tegner, C., Namur, O. & Pilbeam, L. (2015). The earliest history of the Skaergaard magma chamber: a textural and geochemical study of the Cambridge drill core. *Journal of Petrology* **56**, 1199–1227.
Holness, M. B., Tegner, C., Nielsen, T. F. D. & Charlier, B. (2017a). The thickness of the mushy layer on the floor of the Skaergaard magma chamber at apatite saturation. *Journal of Petrology* **58**, 909–932.
Holness, M. B., Tegner, C., Nielsen, T. F. D., Stripp, G. & Morse, S. A. (2007b). A textural record of solidification and cooling in the Skaergaard intrusion, East Greenland. *Journal of Petrology* **48**, 2359–2377.
Holness, M. B., Stripp, G., Humphreys, M. C. S., Veksler, I. V., Nielsen, T. F. D. & Tegner, C. (2011). Silicate liquid immiscibility within the crystal mush: late-stage magmatic microstructures in the Skaergaard intrusion, East Greenland. *Journal of Petrology* **52**, 175–222.

Holycross, M. E. & Watson, E. B. (2016). Diffusive fractionation of trace elements in basaltic melt. *Contributions to Mineralogy and Petrology* **171**, 80.

Hoover, J. D. (1989). Petrology of the Marginal Border Series of the Skaergaard intrusion. *Journal of Petrology* **30**, 399–439.

Horn, I., Hinton, R. W., Jackson, S. E. & Longerich, H. P. (1997). Ultra-trace element analysis of NIST SRM 616 and 614 using laser ablation microprobe-inductively coupled plasma-mass spectrometry (LAM-ICP-MS): a comparison with secondary ion mass spectrometry (SIMS). *Geostandards and Geoanalytical Research* **21**, 191–203.

Humphreys, M. C. S. (2009). Chemical evolution of intercumulus liquid, as recorded in plagioclase overgrowth rims from the Skaergaard intrusion. *Journal of Petrology* **50**, 127–145.

Humphreys, M. C. S. (2011). Silicate liquid immiscibility within the crystal mush: evidence from Ti in plagioclase from the Skaergaard intrusion. *Journal of Petrology* **52**, 147–174.

Hunter, R. H. & Sparks, R. S. J. (1987). The differentiation of the Skaergaard intrusion. *Contributions to Mineralogy and Petrology* **95**, 451–461.

Irvine, T. N. (1980). Magmatic infiltration metasomatism, double-diffusive fractional crystallization, and adcumulus growth in the Muskox intrusion and other layered Intrusions. In: Hargraves, R. B., (ed.) *Physics of Magmatic Processes*. Princeton, NJ: Princeton University Press, pp. 325–384.

Jakobsen, J. K., Veksler, I. V., Tegner, C. & Brooks, C. K. (2005). Immiscible iron- and silica-rich melts in basalt petrogenesis documented in the Skaergaard intrusion. *Geology* **33**, 885–888.

Jakobsen, J. K., Veksler, I. V., Tegner, C. & Brooks, C. K. (2011). Crystallization of the Skaergaard intrusion from an emulsion of immiscible iron- and silica-rich liquids: evidence from melt inclusions in plagioclase. *Journal of Petrology* **52**, 345–373.

Jang, Y. D. (2001). Differentiation trend of rare earth elements of the Skaergaard intrusion. *Economic and Environmental Geology* **34**, 617–625.

Jang, Y. D. & Naslund, H. R. (2001). Major and trace element composition of Skaergaard plagioclase: geochemical evidence for changes in magma dynamics during the final stage of crystallization of the Skaergaard Intrusion. *Contributions to Mineralogy and Petrology* **140**, 441–457.

Jang, Y. D., Naslund, H. R. & McBirney, A. R. (2001). The differentiation trend of the Skaergaard intrusion and the timing of magnetite crystallization: iron enrichment revisited. *Earth and Planetary Science Letters* **189**, 189–196.

Jaupart, C. & Tait, S. (1995). Dynamics of differentiation in magma reservoirs. *Journal of Geophysical Research* **100**, 17615–17636.

Jerram, D. A., Cheadle, M. J. & Philpotts, A. R. (2003). Quantifying the building blocks of igneous rocks: are clustered crystal frameworks the foundation? *Journal of Petrology* **44**, 2033–2051.

Jochum, K. P., Pfander, J., Woodhead, J. D., Willbold, M., Stoll, B., Herwig, K., Amini, M., Abouchami, W. & Hofmann, A. W. (2005). MPI-DING glasses: new geological reference materials for in situ Pb isotope analysis. *Geochemistry, Geophysics, Geosystems* **6**, Q10008.

Keays, R. R. & Tegner, C. (2016). Magma chamber processes in the formation of the low-sulphide magmatic Au-PGE mineralization of the Platinova Reef in the Skaergaard intrusion, East Greenland. *Journal of Petrology* **56**, 2319–2340.

Kerr, R. C. (1995). Convective crystal dissolution. *Contributions to Mineralogy and Petrology* **121**, 237–246.

Kovalenko, V. I., Hervig, R. L. & Sheridan, M. F. (1988). Ion-microprobe analyses of trace elements in anorthoclase, hedenbergite, aenigmatite, quartz, apatite, and glass in pantellerite: evidence for high water contents in pantellerite melt. *American Mineralogist* **73**, 1038–1045.

Kuritani, T., Yokoyama, T. and Nakamura, E. (2007). Rates of thermal and chemical evolution of magmas in a cooling magma chamber: a chronological and theoretical study on basaltic and andesitic lavas from Rishiri volcano, Japan. *Journal of Petrology* **48**, 1295–1319.

Langmuir, C. H. (1989). Geochemical consequences of in situ crystallization. *Nature* **340**, 199–205.

Larsen, R. B., Brooks, C. K. & Bird, D. K. (1992). Methane-bearing, aqueous, saline solutions in the Skaergaard intrusion, East Greenland. *Contributions to Mineralogy and Petrology* **112**, 428–437.

Lissenberg, C. J., MacLeod, C. J., Howard, K. A. & Godard, M. (2013). Pervasive reactive melt migration through fast-spreading lower oceanic crust (Hess Deep, equatorial Pacific Ocean). *Earth and Planetary Science Letters* **361**, 436–447.

Marsh, B. D. (2006). Dynamics of magmatic systems. *Elements* **2**, 287–292.

Mathez, E. (1995). Magmatic metasomatism and formation of the Merensky Reef, Bushveld Complex. *Contributions to Mineralogy and Petrology* **119**, 277–286.

McBirney, A. R. (1989). The Skaergaard Layered Series: I. Structure and average compositions. *Journal of Petrology* **30**, 363–397.

McBirney, A. R. (1996). The Skaergaard intrusion. In: Cawthorn, R. G. (ed.) *Layered Intrusions*. Amsterdam: Elsevier, pp. 147–180.

McBirney, A. R. (1998). The Skaergaard layered series. Part VI. Included trace elements. *Journal of Petrology* **39**, 255–276.

McBirney, A. R. (2002). The Skaergaard layered series. Part VI. Excluded trace elements. *Journal of Petrology* **43**, 535–556.

McBirney, A. R. & Naslund, H. R. (1990). The differentiation of the Skaergaard intrusion, a discussion of Hunter and Sparks (Contributions to Mineralogy and Petrology 95: 451-461). *Contributions to Mineralogy and Petrology* **104**, 235–240.

McBirney, A. R. & Noyes, M. N. (1979). Crystallisation and layering of the Skaergaard intrusion. *Journal of Petrology* **20**, 487–554.

McBirney, A. R. & Sonnenthal, E. L. (1990). Metasomatic replacement in the Skaergaard intrusion, East Greenland: preliminary observations. *Chemical Geology* **88**, 245–260.

McKenzie, D. (1984). The generation and compaction of partially molten rock. *Journal of Petrology* **25**, 713–765.

McKenzie, D. (2011). Compaction and crystallization in magma chambers: towards a model of the Skaergaard intrusion. *Journal of Petrology* **52**, 905–930.

Meurer, W. P. & Claeson, D. T. (2002). Evolution of crystallizing interstitial liquid in an arc-related cumulate determined by LA ICP-MS mapping of a large amphibole oikocryst. *Journal of Petrology* **43**, 607–629.

Meurer, W. P. & Meurer, M. E. S. (2006). Using apatite to dispel the "trapped liquid" concept and to understand the loss of interstitial liquid by compaction in mafic cumulates: an example from the Stillwater Complex, Montana. *Contributions to Mineralogy and Petrology* **151**, 187–201.

Morse, S. A. (1986). Convection in aid of adcumulus growth. *Journal of Petrology* **27**, 1183–1214.

Morse, S. A. (2011). The fractional latent heat of crystallizing magmas. *American Mineralogist* **96**, 682–689.

Morse, S. & Allaz, J. (2013). Experimental partitioning of Sr and Ba in Kiglapait feldspars. *American Mineralogist* **98**, 2197–2200.

Morse, S. & Nolan, K. M. (1984). Origin of strongly reversed rims on plagioclase in cumulates. *Earth and Planetary Science Letters* **68**, 485–498.

Morse, S. & Nolan, K. M. (1986). Kiglapait geochemistry: VII: yttrium and rare earth elements. *Geochimica et Cosmochimica Acta* **49**, 1621–1644.

Namur, O. & Charlier, B. (2012). Efficiency of compaction and compositional convection during mafic crystal mush solidification: the Sept Iles layered intrusion, Canada. *Contributions to Mineralogy and Petrology* **163**, 1049–1068.

Namur, O., Charlier, B. & Holness, M. B. (2012a). Dual origin of Fe–Ti–P gabbros by immiscibility and fractional crystallization of evolved tholeiitic basalts in the Sept Iles layered intrusion. *Lithos* **154**, 100–114.

Namur, O., Charlier, B., Pirard, C., Hermann, J., Liégeois, J. P. & Vander Auwera, J. (2011). Anorthosite formation by plagioclase flotation in ferrobasalt and implications for the lunar crust. *Geochimica et Cosmochimica Acta* **75**, 4998–5018.

Namur, O., Charlier, B., Toplis, M. J. & Vander Auwera, J. (2012b). Prediction of plagioclase-melt equilibria in anhydrous silicate melts at 1-atm. *Contributions to Mineralogy and Petrology* **163**, 133–150.

Namur, O., Humphreys, M. C. S. & Holness, M. B. (2013). Lateral reactive infiltration in a vertical gabbroic crystal mush, Skaergaard intrusion, East Greenland. *Journal of Petrology* **54**, 985–1016.

Namur, O., Humphreys, M. C. S. & Holness, M. B. (2014). Crystallization of interstitial liquid and latent heat buffering in solidifying gabbros: Skaergaard intrusion, Greenland. *Journal of Petrology* **55**, 1389–1427.

Namur, O., Abily, B., Boudreau, A. E., Blanchette, F., Bush, J. W. M., Ceuleneer, G., Charlier, B., Donaldson, C. H., Duchesne, J.-C., Higgins, M. D., Morata, D., Nielsen, T. F. D., O'Driscoll, B., Pang, K. N., Peacock, T., Spandler, C. J., Toramaru, A. & Veksler, I. (2015). Igneous layering in basaltic magma chambers. In: Charlier, B., Namur, O., Latypov, R., & Tegner, C. (eds) *Layered Intrusions*. Netherlands: Springer, pp. 75–152.

Nash, W. (1976). Fluorine, chlorine, and OH-bearing minerals in the Skaergaard intrusion. *American Journal of Science* **276**, 546–556.

Naslund, H. R. (1984). Petrology of the Upper Border Series of the Skaergaard intrusion. *Journal of Petrology* **25**, 185–212.

Nielsen, T. F. D. (2004). The shape and volume of the Skaergaard intrusion, Greenland: implications for mass balance and bulk composition. *Journal of Petrology* **45**, 507–530.

Nielsen, T. F. D., Olsen, S. D. & Stensgaard, B. M. (2009). Developing a 3-D model for the Skaergaard intrusion in East Greenland: constraints on structure, mineralisation and petrogenetic models. *Geological Survey of Denmark and Greenland Bulletin* **17**, 61–64.

Nielsen, T. F. D., Andersen, J. C., Holness, M. B., Keiding, J. K., Rudashevsky, N. S., Rudashevsky, V. N., Salmonsen, L. P., Tegner, C. & Veksler, I. V. (2015). The Skaergaard PGE and gold deposit: the result of in situ fractionation, sulphide saturation, and magma chamber-scale precious metal redistribution by immiscible Fe-rich melt. *Journal of Petrology* **56**, 1643–1676.

Norman, M. D., Griffin, W. L., Pearson, N. J., Garcia, M. O. & O'Reilly, S. Y. (1998). Quantitative analysis of trace element abundances in glasses and minerals: a comparison of laser ablation inductively coupled plasma mass spectrometry, solution inductively coupled plasma mass spectrometry, proton microprobe and electron microprobe data. *Journal of Analytical Atomic Spectrometry* **13**, 477–482.

Nwe, Y. Y. (1976). Electron-probe studies of the earlier pyroxenes and olivines from the Skaergaard intrusion, East Greenland. *Contributions to Mineralogy and Petrology* **55**, 105–126.

O'Reilly, S. Y. & Griffin, W. (1988). Mantle metasomatism beneath western Victoria, Australia: I. Metasomatic processes in Cr-diopside lherzolites. *Geochimica et Cosmochimica Acta* **52**, 433–447.

Pearce, N. J., Perkins, W. T., Westgate, J. A., Gorton, M. P., Jackson, S., Neal, C. R. & Chenery, S. P. (1997). A compilation of new and published major and trace element data for NIST SRM 610 and NIST SRM 612 glass reference materials. *Geostandards and Geoanalytical Research* **21**, 115–144.

Philpotts, A. R., Shi, J. & Brustman, C. (1998). Role of plagioclase crystal chains in the differentiation of partly crystallized basaltic magma. *Nature* **395**, 343–346.

Prowatke, S. & Klemme, S. (2006). Trace element partitioning between apatite and silicate melts. *Geochimica et Cosmochimica Acta* **70**, 4513–4527.

Roex, A. & Class, C. (2016). Metasomatic enrichment of Proterozoic mantle south of the Kaapvaal Craton, South Africa: origin of sinusoidal REE patterns in clinopyroxene and garnet. *Contributions to Mineralogy and Petrology* **171**, 1–24.

Ross, K. & Elthon, D. (1997). Cumulus and postcumulus crystallization in the oceanic crust: major- and trace-element geochemistry of Leg 153 gabbroic rocks. *Proceedings—Ocean Drilling Program Scientific Results*, vol. 153. College Station: Texas A&M University. pp. 333–350.

Salmonsen, L. P. & Tegner, C. (2013). Crystallization sequence of the Upper Border Series of the Skaergaard intrusion: revised subdivision and implications for chamber-scale magma homogeneity. *Contributions to Mineralogy and Petrology* **165**, 1155–1171.

Schmidt, M. W., Connolly, J. A. D., Gunther, D. & Bogaerts, M. (2006). Element partitioning: the role of melt structure and composition. *Science* **312**, 1646–1650.

Sun, C. & Liang, Y. (2012). Distribution of REE between clinopyroxene and basaltic melt along a mantle adiabat: effects of major element composition, water, and temperature. *Contributions to Mineralogy and Petrology* **163**, 807–823.

Sun, C. & Liang, Y. (2017). A REE-in-plagioclase–clinopyroxene thermometer for crustal rocks. *Contributions to Mineralogy and Petrology* **172**, 24.

Sun, C., Graff, M. & Liang, Y. (2017). Trace element partitioning between plagioclase and silicate melt: the importance of temperature and plagioclase composition, with implications for terrestrial and lunar magmatism. *Geochimica et Cosmochimica Acta* **206**, 273–295.

Sun, S. S. & McDonough, W. F. (1989). Chemical and isotopic systematics of oceanic basalts: im- plication for mantle composition and process. In: Saunders, A. D. & Norry, M. J. (eds) *Magmatism in the Ocean Basins*, Vol. 42. London: Geological Society of London Special Publications, pp. 313–345.

Tait, S. R., Huppert, H. E. & Sparks, R. S. J. (1984). The role of compositional convection in the formation of adcumulus rocks. *Lithos* **17**, 139–146.

Tanner, D., Mavrogenes, J. A., Arculus, R. J. & Jenner, F. E. (2014). Trace element stratigraphy of the Bellevue core, Northern Bushveld: multiple magma injections obscured by diffusive processes. *Journal of Petrology* **55**, 859–882.

Tegner, C. (1997). Iron in plagioclase as a monitor of the differentiation of the Skaergaard intrusion. *Contributions to Mineralogy and Petrology* **128**, 45–51.

Tegner, C., Lesher, C., Larsen, L. & Watt, W. (1998). Evidence from the rare-earth-element record of mantle melting for cooling of the tertiary Iceland plume. *Nature* **395**, 591–594.

Tegner, C., Thy, P., Holness, M. B., Jakobsen, J. K. & Lesher, C. E. (2009). Differentiation and compaction in the Skaergaard intrusion. *Journal of Petrology* **50**, 813–840.

Thy, P., Lesher, C. & Tegner, C. (2009a). The Skaergaard liquid line of descent revisited. *Contributions to Mineralogy and Petrology* **157**, 735–747.

Thy, P., Tegner, C. & Lesher, C. E. (2009b). Liquidus temperatures of the Skaergaard magma. *American Mineralogist* **94**, 1371–1376.

Thy, P., Lesher, C. E., Nielsen, T. F. D. & Brooks, C. K. (2006). Experimental constraints on the Skaergaard liquid line of descent. *Lithos* **92**, 154–180.

Tollari, N., Toplis, M. J. & Barnes, S. J. (2006). Predicting phosphate saturation in silicate magmas: an experimental study of the effects of melt composition and temperature. *Geochimica et Cosmochimica Acta* **70**, 1518–1536.

Toplis, M. & Corgne, A. (2002). An experimental study of element partitioning between magnetite, clinopyroxene and iron-bearing silicate liquids with particular emphasis on vanadium. *Contributions to Mineralogy and Petrology* **144**, 22–37.

Toplis, M., Brown, W. & Pupier, E. (2008). Plagioclase in the Skaergaard intrusion. Part 1: core and rim compositions in the layered series. *Contributions to Mineralogy and Petrology* **155**, 329–340.

Toplis, M. J. & Carroll, M. R. (1995). An experimental study of the influence of oxygen fugacity on FeTi oxide stability, phase relations, and mineral-melt equilibria in ferro-basaltic systems. *Journal of Petrology* **36**, 1137–1170.

Toplis, M. J. & Carroll, M. R. (1996). Differentiation of ferro-basaltic magmas under conditions closed and open to oxygen: implications for the Skaergaard intrusion and other natural systems. *Journal of Petrology* **37**, 837–858.

Tribuzio, R., Renna, M. R., Braga, R. & Dallai, L. (2009). Petrogenesis of Early Permian olivine-bearing cumulates and associated basalt dykes from Bocca di Tenda (Northern Corsica): implications for post-collisional Variscan evolution. *Chemical Geology* **259**, 190–203.

Tribuzio, R., Tiepolo, M., Vannucci, R. & Bottazzi, P. (1999). Trace element distribution within olivine-bearing gabbros from the Northern Apennine ophiolites (Italy): evidence for post-cumulus crystallization in MOR-type gabbroic rocks. *Contributions to Mineralogy and Petrology* **134**, 123–133.

Van Orman, J. A., Grove, T. L. & Shimizu, N. (2001). Rare earth element diffusion in diopside: influence of temperature, pressure, and ionic radius, and an elastic model for diffusion in silicates. *Contributions to Mineralogy and Petrology* **141**, 687–703.

VanTongeren, J. A., Kelemen, P. B. & Hanghoj, K. (2008). Cooling rates in the lower crust of the Oman ophiolite: Ca in olivine, revisited. *Earth and Planetary Science Letters* **267**, 69–82.

Veksler, I. V. & Charlier, B. (2015). Silicate liquid immiscibility in layered Intrusions. In: Charlier, B., Namur, O., Latypov, R., & Tegner, C. (eds) *Layered Intrusions*. Netherlands: Springer, pp. 229–258.

Veksler, I., Dorfman, A., Danyushevsky, L., Jakobsen, J. & Dingwell, D. (2006). Immiscible silicate liquid partition coefficients: implications for crystal-melt element partitioning and basalt petrogenesis. *Contributions to Mineralogy and Petrology* **152**, 685–702.

Villemant, B. (1988). Trace element evolution in the Phlegrean Fields (Central Italy): fractional crystallization and selective enrichment. *Contributions to Mineralogy and Petrology* **98**, 169–183.

Wager, L. R. & Brown, G. M. (1968). *Layered Igneous Rocks*, Edinburgh: Oliver & Boyd.

Wager, L. R., Brown, G. M. & Wadsworth, W. J. (1960). Types of igneous cumulates. *Journal of Petrology* **1**, 73–85.

Watson, E. B. & Green, T. H. (1981). Apatite/liquid partition coefficients for the rare earth elements and strontium. *Earth and Planetary Science Letters* **56**, 405–421.

Wood, B. J. & Blundy, J. (1997). A predictive model for rare earth element partitioning between clinopyroxene and anhydrous silicate melt. *Contributions to Mineralogy and Petrology* **129**, 166–181.

Zajacz, Z., Halter, W. E., Pettke, T. & Guillong, M. (2008). Determination of fluid/melt partition coefficients by LA-ICPMS analysis of co-existing fluid and silicate melt inclusions: controls on element partitioning. *Geochimica et Cosmochimica Acta* **72**, 2169–2197.

Zhang, Y., Ni, H. & Chen, Y. (2010). Diffusion data in silicate melts. *Reviews in Mineralogy and Geochemistry* **72**, 311–408.